Three-dimensional flow structure and bed morphology in large elongate meander loops with different outer bank roughness characteristics

Kory M. Konsoer[a,b,*], Bruce L. Rhoads[c], James L. Best[d], Eddy J. Langendoen[e], Jorge D. Abad[f], Dan R. Parsons[g], Marcelo H. Garcia[h]

Affiliations

[a] Department of Geography and Anthropology, Louisiana State University, USA

[b] Coastal Studies Institute, Louisiana State University, USA

[c] Department of Geography and Geographic Information Science, University of Illinois, Urbana-Champaign, USA

[d] Departments of Geology, Geography and Geographic Information Science, Mechanical Science and Engineering, and Ven Te Chow Hydrosystems Laboratory, University of Illinois, Urbana-Champaign, USA

[e] US Dept. of Agriculture, Agricultural Research Service, National Sedimentation Laboratory

[f] Department of Civil and Environmental Engineering, University of Pittsburgh, USA

[g] Department of Geography, Environment, and Earth Sciences, University of Hull, UK

[h] Department of Civil and Environmental Engineering, Ven Te Chow Hydrosystems Laboratory, University of Illinois, USA

***Corresponding Author.**

E-mail addresses: kkonsoer@lsu.edu (K.M. Konsoer)

Key Points:

1) 3D flow structure is characterized by topographic steering by the point bar and by curvature-induced helical motion

2) Bed morphology in large elongate loops in natural rivers differs from shingle bar topography in experimental channels
3) Differences in outer bank roughness produce differences in the relative magnitude and variability of near-bank velocities

Abstract:

Although the dynamics of meandering rivers have been the focus of considerable research, few studies have examined the three-dimensional flow structure and bed morphology within elongate loops of large meandering channels. The present study focuses on the spatial patterns of three-dimensional flow structure and bed morphology within two elongate loops along the Wabash River, USA. It also examines how differences in outer bank roughness influence near-bank flow characteristics within these loops. The outer bank of one of the loops is forested with abundant large woody debris, whereas the outer bank of the other loop is unforested and lacks large woody debris. Bedrock is present locally in the banks and beds of both bends. Velocities were measured along cross sections oriented perpendicular to the channel centerline using a boat-mounted acoustic Doppler current profiler during two different events – a near-bankfull flow and an overbank flow event that extensively inundated the floodplain. Detailed channel bathymetry and bedform geometry were obtained using a multibeam echo sounder during the near-bankfull event. Flow structure within the loops is characterized by strong topographic steering by the point bar, by the development of helical motion associated with flow curvature, and by acceleration of flow where bedrock is exposed along the outer bank. Near-bank velocities during the overbank event are less than those for the near-bankfull flow, highlighting the strong influence of the point bar on redistribution of mass and momentum of the flow at sub-bankfull stages. Multiple outer bank pools are evident within the unforested elongate meander loop, but the forested loop lacks multiple pools, which may reflect the influence of abundant large woody debris on near-bank velocity characteristics. The positions of pools within both loops can be linked to spatial variations in planform curvature. The findings indicate that flow structure and bed morphology in these large

elongate loops is similar to that in small elongate loops, but differs somewhat from flow structure and bed morphology reported for experimental elongate loops.

1. Introduction

The meandering of alluvial rivers is the result of complex interactions among three-dimensional flow structure, channel topography, sediment transport, and the geotechnical properties of the channel banks and floodplain. Past research on meandering rivers has focused largely on simple bends, in which the chord length, *C*, between points of inflection (zero channel curvature) at the upstream and downstream ends of the bend exceeds the radius of curvature of the bend, and in which the sum of the absolute values of angles of the channel path relative to the chord orientation, α_S, does not exceed 180^o (Frothingham and Rhoads, 2003). As flow enters a simple bend, an outward-directed centrifugal force causes super-elevation of the water surface along the outer bank, which generates an opposing inward-directed pressure gradient force. The local imbalance between these two forces over the flow depth results in large-scale helical motion (Dietrich, 1987). Secondary circulation associated with the helical motion advects high momentum near-surface fluid outward and downward within the curving channel, resulting in the development of a submerged high-velocity core near the base of the outer (concave) bank (Thorne *et al.*, 1985; Blanckaert, 2011). The development of a point bar within natural meandering channels also modifies the lateral extent of secondary circulation, confining it to the channel thalweg through the effects of topographic steering (Dietrich and Smith, 1983; Rhoads and Welford, 1991; Blanckaert, 2010).

Much less work has examined the structure of flow and bed morphology within elongate meander loops. Here, the planform geometry is characterized by a chord length that is less than the perpendicular distance, *P*, from the chord to the loop apex, and by a value of α_S that exceeds 180^o (Frothingham and Rhoads, 2003). Experimental work has shown that the bed morphology in elongate loops displays multiple outer bank pools and inner bank bars, commonly referred to as shingle bars (Whiting and Dietrich, 1993a,b; Termini, 2009; Abad and Garcia, 2009b; Termini and Piraino, 2011). In the case of symmetrical loops, the first outer bank pool is typically located where a line projected tangentially from the upstream inner bank intersects the outer bank. At this location, the core of maixmum velocity often shifts from the inner bank to near the outer bank (Whiting and Dietrich, 1993a; Termini, 2009). For asymmetrically skewed, or Kinoshita, loops, experimental work has shown that the orientation of the bend skewness influences the flow structure and bed morphology throughout the bend (Abad and Garcia, 2009b). For upstream-skewed conditions, the zone of maximum scour along the outer bank occurs upstream of the bend apex, whereas for downstream-skewed conditions the locus of maximum scour along the outer bank is downstream of the bend apex (Abad and Garcia, 2009b). Also, the spatial extent of the inner bank bar for downstream-skewed bends is shifted upstream relative to the case for upstream-skewed bends. In addition to steady bars and pools, the bed morphology in experimental elongate bends is characterized by mesoscale bedforms (dunes) that migrate through the bend, producing a time-dependent variation in the bed morphology, which can reinforce or diminish variability associated with the steady signature of topography (Abad and Garcia, 2009b).

Field observations of flow and bed morphology within elongate meander loops have focused mainly on asymmetrically-skewed planform configurations (Jackson, 1975a,b). Whereas patterns of flow structure from field studies in asymmetrical elongate loops are in general agreement with findings from experimental channels (Jackson, 1975; Abad and Garcia, 2009a,b), field studies have yet to document the presence of well-defined shingle bars in large elongate meander loops. Detailed field studies of the co-evolution of three-dimensional flow structure and channel morphology in compound meander loops, defined as loops that exhibit two or more offset lobes of curvature (Frothingham and Rhoads, 2003), have documented multiple outer bank pools that correspond locally with zones of accelerated bank retreat (Hooke and Harvey, 1983; Frothingham and Rhoads, 2003; Engel and Rhoads, 2012). As flow moves through a compound loop, helical motion generated by spatially varying curvature, along with steering of the flow by the point bar, shifts the core of maximum velocity outwards toward the apex of each lobe of curvature and in loops of high curvature can even result in flow separation along the inner bank (Ferguson *et al*,. 2003). Between these lobes, helical motion decays as a result of reductions in channel curvature (Hooke and Harvey, 1983; Frothingham and Rhoads, 2003). The development and decay of secondary flow through compound loops leads to spatial variation in erosion and deposition, the formation of a secondary inflection point, and continued distortion of the loop planform over time (Harvey and Hooke, 1983; Frothingham and Rhoads, 2003; Engel and Rhoads, 2012).

The lack of detailed process-based investigations of elongate meander loops, particularly in large rivers, limits understanding of the dynamics of complex bend geometries and accurate predictions of planform evolution of meandering rivers. To contribute to this research need, the aims of the present paper are to: 1) characterize the three-dimensional flow structure and bed morphology within two elongate meander loops with different outer bank roughness characteristics, and 2) compare these results to previous experimental and field studies of flow and bed morphology in bends with simple and complex planform geometries. The results provide insight into the influences of topographic steering, planform curvature, hydrologic variability, large woody debris, and exposed bedrock on spatial patterns of flow and bed morphology within elongate meander loops.

2. Field Site

The field site consists of two elongate meander loops on the lower Wabash River, roughly 6 km upstream from Grayville, Illinois (Jackson, 1975a; Figure 1). At this location, the Wabash River has a bankfull width of 200 to 350 m, a bankfull depth of 4 to 8 m, and a drainage area of *c.* 74,070 km^2. Based on 85 years of hydrologic data from a U.S. Geological Survey gaging station at Mt. Carmel, Illinois (~20 km upstream of Grayville), the mean annual discharge of the lower Wabash River is 881 m^3s^{-1} with a mean annual peak discharge of 4112 m^3s^{-1}. The lower Wabash River meanders freely across its floodplain, except at several locations where it erodes into Pleistocene glaciofluvial sediments or Carboniferous bedrock (Jackson, 1975a; Konsoer *et al.*, 2015; Figure 2A,B).

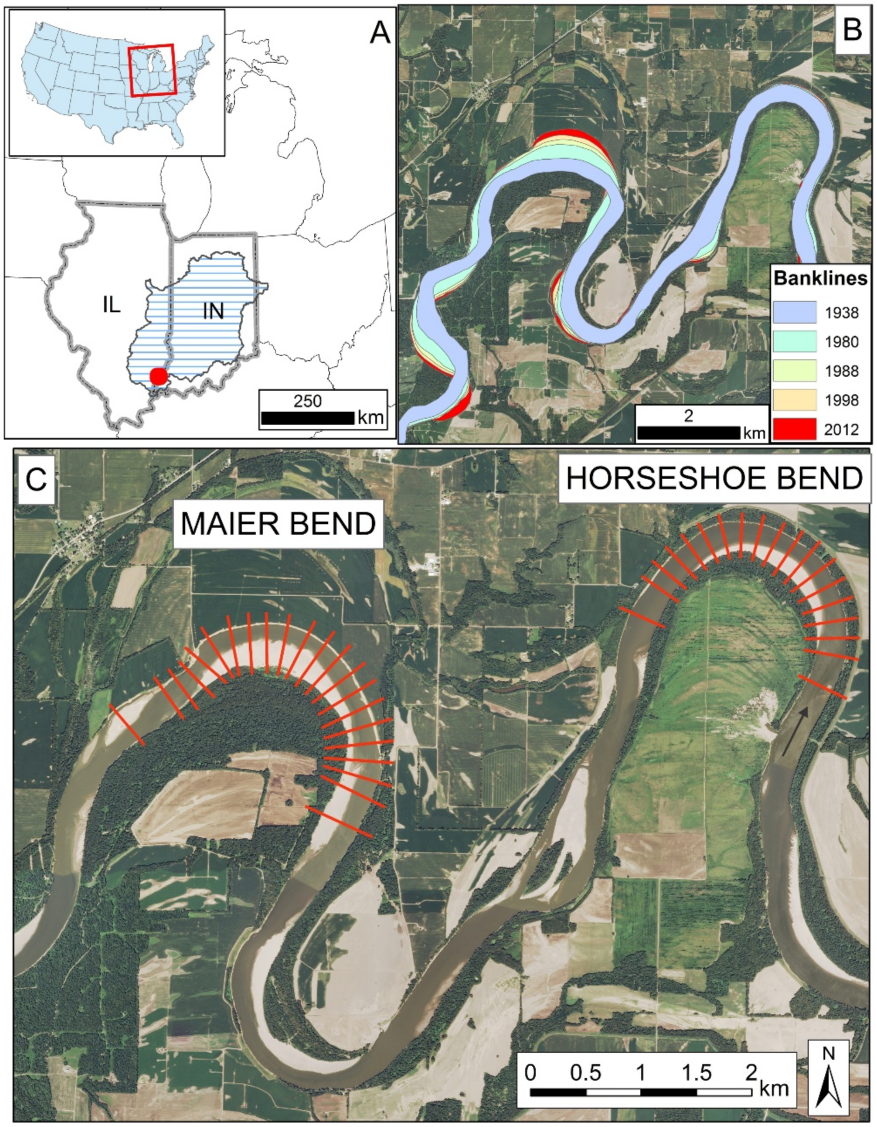

Figure 1. (A) Location of field site within Wabash River basin (blue hatched shading) shown by red dot. (B) Digitized banklines from aerial photography showing patterns of channel migration in the study area for ~74 years. (C) Location of Maier Bend and Horseshoe Bend with ADCP cross sections indicated. Black arrow shows general flow direction.

The upstream site, Horseshoe Bend, is ~3 km in channel length with riparian forest along the outer bank (Figure 2A). Bank materials consist of a relatively thick layer (4-6 m) of cohesive fine sediments (> 70% silt and clay) underlain by a basal layer of coarse sand and fine gravel with median grain size of ~0.4 mm (Konsoer *et al.*, 2015). The upper cohesive material maintains a nearly vertical face, whereas the non-cohesive lower part of the bank tends to be at, or close to, the angle of repose. On the downstream limb of the bend, the channel erodes into Pennsylvanian shales of the Mattoon Formation (Illinois Basin Consortium – Study 5, 2001), restricting downstream migration of the bend (Figure 2A). Erosion of the outer bank supplies large trees to the channel, some of which are embedded in the base of the bank. The embedded trees tend to become aligned approximately parallel to the local mean flow direction, and are present along the majority of the outer bank. Repeat surveys suggest individual embedded trees can have residence times exceeding five years (Konsoer *et al*., 2015). These characteristic lead to an average migration rate for Horseshoe Bend of ~0.75 myr^{-1} (Konsoer *et al*., 2015).

The second site, Maier Bend, located ~12 km downstream of Horseshoe Bend, is ~4 km in length. No tributaries join the river between these two bends. The outer bank of Maier Bend is mainly unvegetated and flanked by agricultural fields (Figure 2B) in which corn and soybeans are grown. In contrast to Horseshoe Bend, the bank material at Maier Bend is composed of a lower layer consisting of 4-5 m of coarse sand and fine gravel with a median grain size of ~1.0 mm (Konsoer *et al*., 2015). This part of the bank has a slope angle of *c*. 30°. The non-cohesive sediment composition of the banks and shallow-rooted crops along the outer bank contribute to an average outer bank migration rate ~10-12 myr^{-1} (Konsoer *et al*., 2015). The upper part of the bank, which is nearly vertical, consists of a 1-2 m layer of fine sand and silt. The outer bank morphology includes large-scale embayments (15-30 m) spaced irregularly along the bend. Downstream of the bend apex, the channel erodes into a low outcrop of interbedded shales and sandstones of the Pennsylvanian Bond Formation (Illinois Basin Consortium – Study 5, 2001; Figure 2B), exposing bedrock in the channel bed and lower part of the outer bank.

Figure 2: (A) Photograph looking upstream on Horseshoe Bend at low flow showing forested outer banks and the outcrop of bedrock (note detached slabs of rock on the bedrock surface). (B) Photograph looking downstream on Maier Bend showing a lack of vegetation on the banks and a local bedrock platform at the base of the outer bank.

3. Methods

The planform characteristics of Maier and Horseshoe bends were examined by digitizing both channel banklines from 2011 National Agriculture Imagery Program (NAIP) orthophotographs and using the Channel Planform Statistics Toolbox (Lauer, 2012) to interpolate the channel centerline, which provided the basis for establishing a streamwise (*s*) and cross-stream (*n*) coordinate system for each loop. A centerline curvature series was then calculated using the Matlab script PCS-Curvature (Guneralp and Rhoads, 2008), which was used to determine the *s* coordinates of inflection points and the average radius of curvature for each bend. The inflection coordinates and radius of curvature were overlain on the NAIP 2011 orthophotograph basemap, and the chord length, perpendicular distance from the chord to the bend apex, and the angles between channel path and chord orientation at inflection points were measured in ArcGIS. Cross sections orthogonal to the centerline were established at a streamwise (*s*) spacing of 150 m, corresponding to the channel half-width (Güneralp and Rhoads, 2008). These cross-sections are labelled by whole number increments, starting with the meander bend upstream of Horseshoe Bend and continuing downstream through Maier Bend.

Flow measurements were obtained during two different flood events in the spring and summer 2011 (Table 1). The first set of measurements (Campaign 1) occurred on May 9-10, 2011 during the receding limb of a flood with a peak discharge of approximately 7,650 m^3s^{-1} (05/03/2011) and a recurrence interval (R.I.) of ~15 years. The discharge during the two days of data acquisition at the two loops produced substantial overbank flow along the Wabash River. The second set of measurements (Campaign 2) occurred on June 28-29, 2011 near peak flow of an event with a maximum discharge of 2450 m^3s^{-1} and R.I. of ~1.2 years. This event closely approximated bankfull discharge along the lower Wabash River. Variations in discharge during the two measurement campaigns were less than 4% and variations in stage were less than 1.6% (Table 1). Thus, flow conditions were remarkably steady for a natural river.

Table 1: Summary of hydrologic conditions during field campaigns. Data obtained from USGS gaging station at Mt. Carmel, IL

Site	Date	Q (m^3s^{-1})	Q_{av} (m3s-1)	% diff Q	S (m)	S_{av} (m)	% diff S
Maier Bend	5/9/2011	6031 - 5805	5918	-3.75	9.49 - 9.37	9.43	-1.26
	6/28/2011	2339 - 2398	2369	2.52	6.33 - 6.43	6.38	1.58
Horseshoe Bend	5/10/2011	5465 - 5267	5366	-3.61	9.18 - 9.06	9.12	-1.31
	6/29/2011	2424 - 2398	2411	-1.07	6.47 - 6.43	6.45	-0.62

Q is range of discharge, Qav is average discharge for measurement campaign, S is range of stage, and Sav is average stage for measurement campaign.

Three-dimensional velocity measurements were obtained along predetermined cross sections oriented perpendicular to the channel centerline using a boat-mounted Teledyne RDI 1200 kHz acoustic Doppler current profiler (ADCP) with an integrated Trimble dGPS antenna located directly above the ADCP. The sampling frequency of the dGPS was ~1 Hz and the horizontal positional accuracy of the GPS was less than 0.60 m. Each cross section was traversed four to six times to ensure accurate time-averaging of the velocity fields (*cf*. Szupiany *et al*., 2007). Each traverse had a duration of approximately 4 minutes. The ADCP is a 4-beam system with a 20° beam angle and a vertical bin dimension in profiling mode as small as 0.1 m. Velocity measurements were acquired with a sampling frequency ~1 Hz with a resolution of roughly 0.01 ms^{-1} and an overall accuracy of +/- 0.25% of the water and boat velocity. For both campaigns, velocity measurements were collected across the entire width of flow along cross sections that had an average streamwise spacing of 150 m (Figure 1).

All velocity measurements were collected using RDI-WinRiver II, which resolves velocities into north, east, and vertical components. The data were exported in ASCII format and processed using the Velocity Mapping Toolbox (VMT), a suite of Matlab-based programs designed for processing and visualization of ADCP data (Parsons *et al*., 2013). VMT projects multiple ADCP traverses onto a common plane of intersection, and spatially and temporally averages the data for visualization of the three-dimensional velocity field within cross sections. A major advantage of VMT is that it can readily analyze the velocity field using various frames of reference for transverse sections through the flow, including cross=stream (i.e. the orientation of the transverse sections orthogonal to the channel centerline), zero net secondary discharge (the transverse section corresponding to the plane of zero net discharge), and Rozovskii (1957; planes orthogonal to the local depth-averaged vector for each vertical profile of velocity measurements) frames of reference. In the present paper, the downstream – cross-stream frame of reference was used to provide a common fixed frame of reference for comparing the characteristics of the three-dimensional flow structure for the two events.

To investigate the influence of bed topography and flow stage on patterns of flow through the bends, the path of the cross-sectional median discharge (Q_{50}) was compared to the path of the channel centerline. To determine the location of the median discharge, each cross section was divided into 1 m wide segments and the unit discharge was calculated for each segment. The unit discharges were then summed across the channel and the transverse location where 50 percent of the flow occurs on each side of that position (Q_{50}) was determined from the summed data.

Detailed channel bathymetry and bed morphology data were obtained in the loops using a multibeam echo sounder (MBES). MBES surveys were performed using a RESON SeaBat 7125SV, dual frequency 200-400 kHz system with an overall depth resolution of ~6 mm and a maximum sampling frequency of 60 Hz. This system utilizes 512 beams over a swath of 128° and is capable of beam steering, allowing for focused acquisition of bathymetric data near the channel thalweg and outer bank regions. The MBES was used with an Applanix POS-MV inertial motion unit to compensate for boat motion. Locational information was provided by a Leica RTK-GPS system. The MBES survey for Maier Bend was obtained on February 2-4, 2012 with a flow discharge of ~2800 m^3s^{-1} (R.I. ~1.3 years), whereas surveys from two campaigns were used for Horseshoe Bend, the first conducted on July 29-31, 2008 (Q ~ 600 m^3s^{-1}, R.I. ~1 year) and the second on January 18, 2013 (Q ~2300 m^3s^{-1}, R.I. ~1.2 years). Post-processing and visualization of the MBES data was performed in Caris HIPS/SIPS software.

4. Results

4.1 Characteristics of meander geometry and curvature

Both bends can be classified as elongate meander loops ($P > C$, $|\alpha_{S1}| + |\alpha_{S2}| > 180°$), with Maier Bend exhibiting ~8.5% more elongation – $(C_m/P_m - C_h/P_h)/C_h/P_h$, where subscripts *m* and *h* correspond to Maier and Horseshoe bends, respectively – than Horseshoe Bend (Figure 3). The curvature series for Maier Bend (Figure 4A,B) shows a pronounced decrease in curvature immediately downstream of the loop apex (*s* ~6000 m), nearly approaching a reversal in curvature (i.e. curvature ~0 at *s* ~7000 m) before increasing and then decreasing again toward the downstream inflection point. This near-reversal of curvature results from the influence of the bedrock outcrop on the planform geometry of the channel that restricts channel migration at this location. In contrast, the curvature series for Horseshoe Bend (Figure 4C,D) is relatively simple, with increasing curvature toward a maximum at the loop apex (*s* ~3650 m) and decreasing curvature to the downstream inflection point. Despite these differences in the spatial pattern of curvature, both loops have similar values of maximum curvature that occur near the apexes (~1.3 x 10^{-3} m^{-1}).

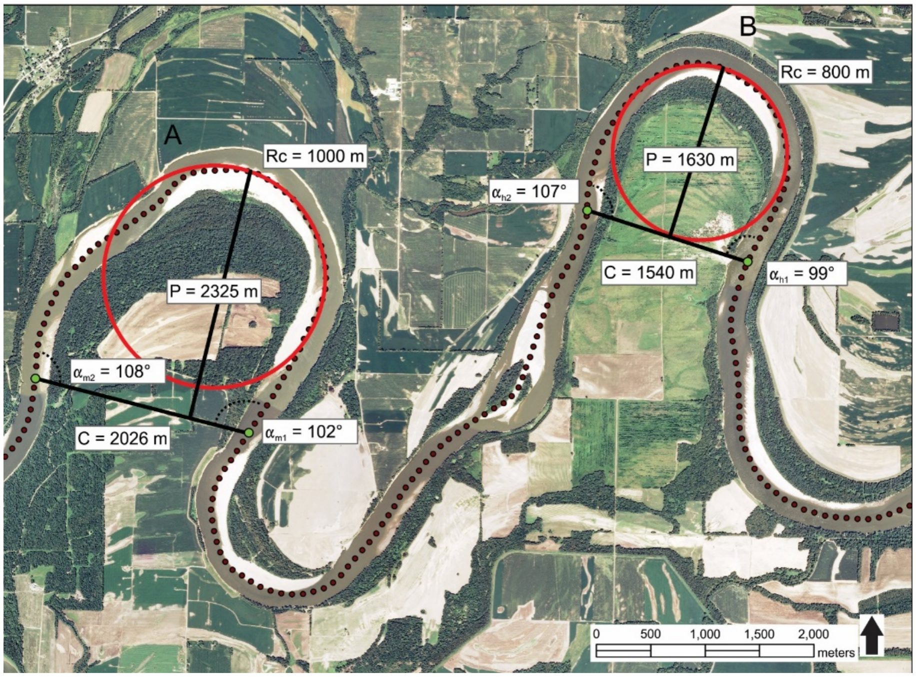

Figure 3: Planform geometric parameters used to classify (A) Maier and (B) Horseshoe bends as elongate meander loops. (*Rc* – radius of curvature; *C* – chord length; *P* – perpendicular distance from chord to loop apex; α – angle between channel path and chord orientation)

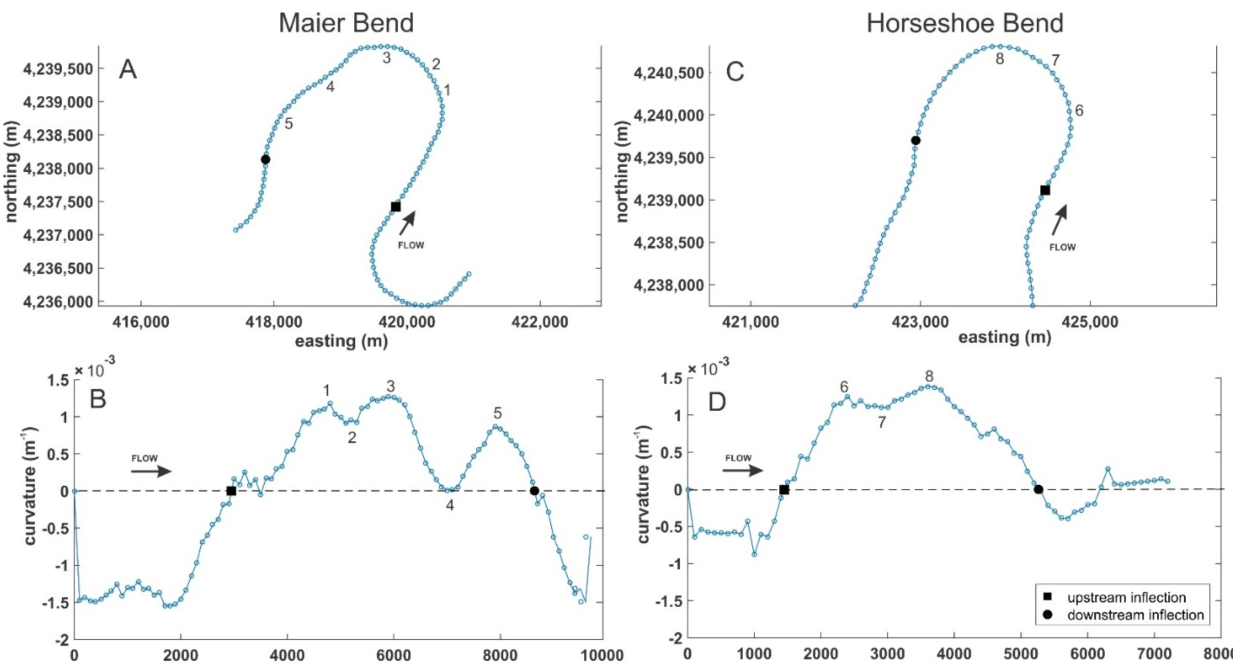

Figure 4: Extracted channel centerlines and curvature series for (A, B) Maier and (C, D) Horseshoe bends. Note the near reversal of curvature in Maier Bend due to bedrock outcrop around streamwise distance ~7000 m. Numbers correspond to locations shown on channel bathymetric maps (Figures 5 and 8).

4.2 Channel bed morphology

The bed morphology of Maier Bend is characterized by a series of pools and bars throughout the meander loop (Figure 5). The first two pools (P1 and P2, Figure 5) are relatively small and located along the outer bank of the upstream limb, directly across from a large gravel bar along the inner bank. A third pool (P3) is located along the outer bank at the bend entrance, whereas the fourth pool (P4) begins upstream of the bend apex and extends downstream past the bedrock outcrop in the downstream limb of the loop (Figure 5). Pools P3 and P4 extend over more than 1000 m and have scour depths up to 12 m below the top of the outer banks. These two pools are separated by a region of higher topography that is approximately 100 m in length (Figure 5). The fourth pool (labeled P4) increases in size immediately downstream of the constriction in channel width associated with the bedrock outcrop along the outer bank. A small fifth pool (P5) is located along the inner bank opposite an outer bank bar that has developed where the channel width increases in the lee of the bedrock outcrop (Figure 5).

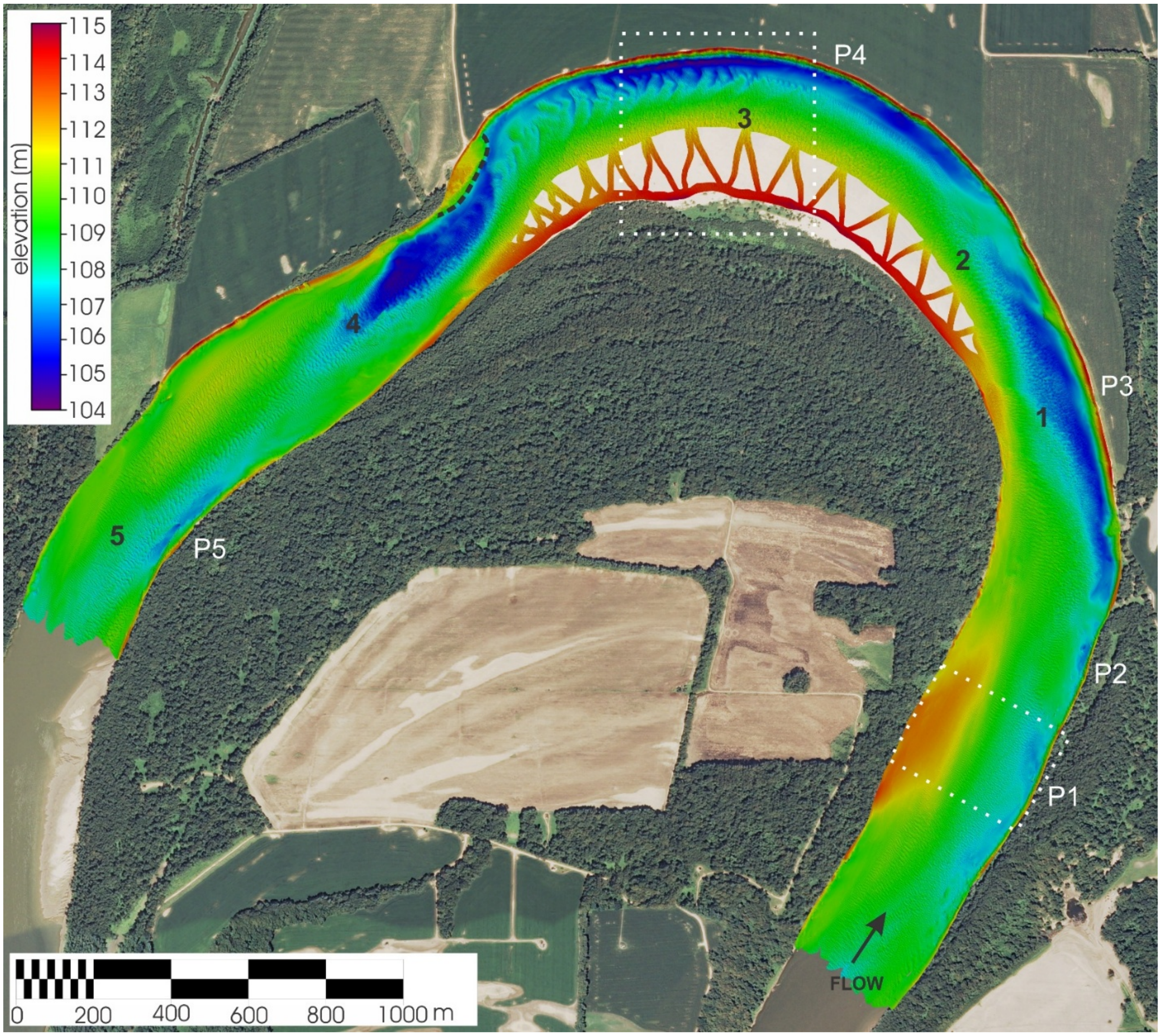

Figure 5: Bathymetric map derived from 2012 multibeam survey (0.5 m horizontal grid resolution) for Maier Bend. White dashed boxes indicate locations of Figures 6 and 7, black dashed line approximates extent of bedrock outcrop, and pools (P) are labeled.

Within the upstream limb of the loop of Maier Bend, bedforms are composed primarily of two-dimensional dunes (Figure 6). The largest bedforms (~7 m wavelength, ~0.75 m amplitude) are located in the outer half of the channel, with the amplitude and wavelength of the bedforms decreasing toward the inner bank. Upstream of the zone of strong channel curvature, isolated barchan dunes of *c*. 0.20 m height are present on the large gravel bar along the inner bank of the loop (Figure 6). The dunes transition into more three-dimensional geometries at, and immediately downstream, of the loop apex where channel curvature increases, and large (amplitude > 1 m) composite dunes are present with maximum wavelengths and amplitues of 50 m and 1.5 m, respectively (Figure 7). These large bedforms become washed out in proximity to the bedrock outcrop, and small bedforms are present near the inner bank adjacent to the bedrock outcrop and within the downstream limb of the loop.

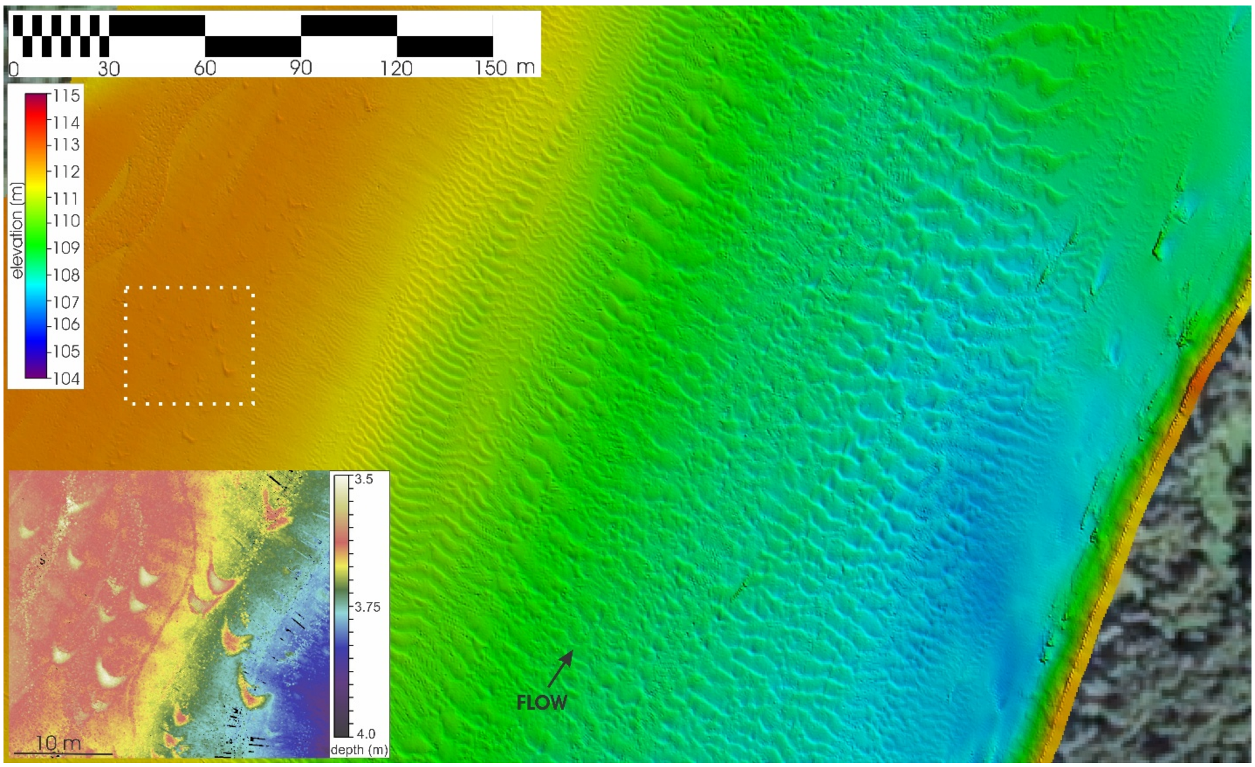

Figure 6: Bathymetric map of upstream limb of Maier Bend (0.5 m horizontal grid resolution) showing transition of bedform geometry from right bank to left bank as described in text (extent of image shown in Figure 5). Inset shows point cloud data that reveal a barchan (sand) dune field on gravel bar substrate (white dashed box indicates location). Note color scale different for insert, with point cloud data ranging from 3.5 – 4.0 m depth.

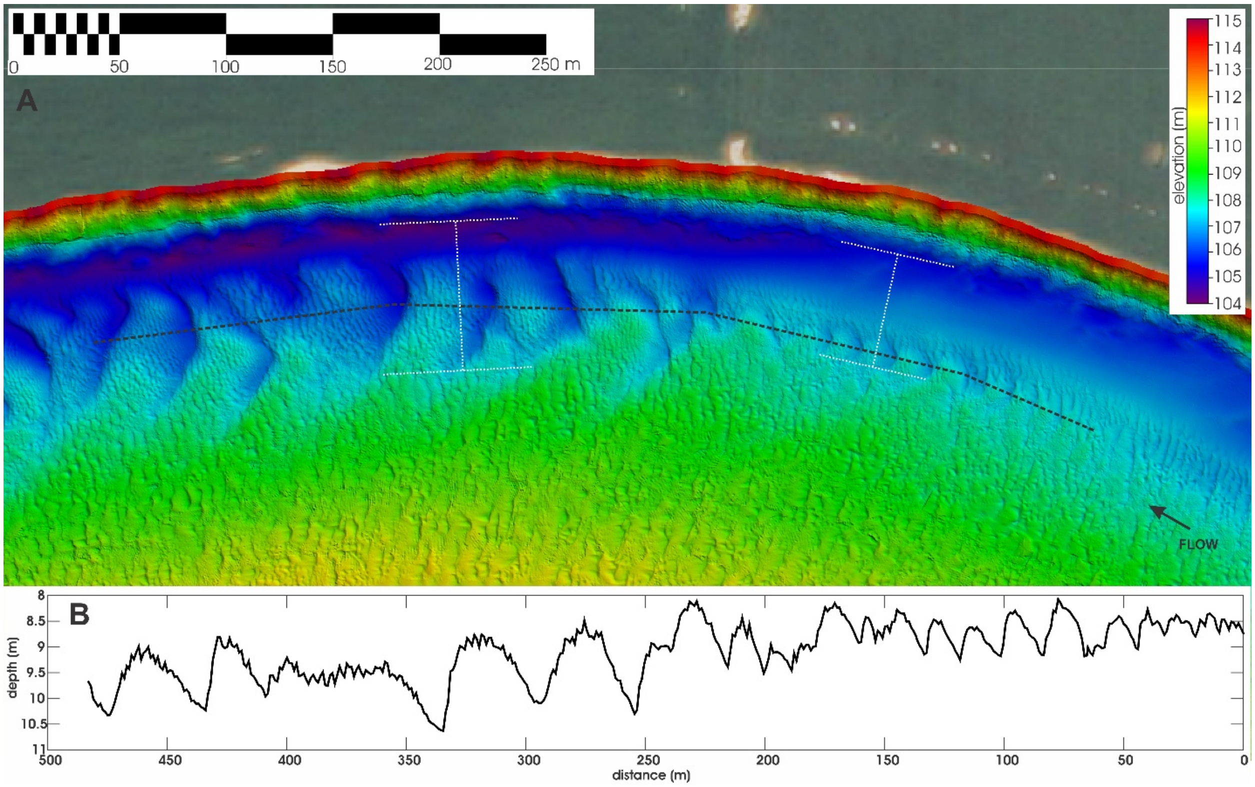

Figure 7: (A) Bathymetric map of Maier Bend (0.5 m resolution) showing bedform geometry immediately upstream and downstream of the loop apex (extent of image shown in Figure 5). (B) Profile of bed topography (dashed line in A) showing the presence of composite dunes and the abrupt increase in bedform wavelength and amplitude downstream of apex, as well as increased scour width (white dashed brackets).

Comparison of overlapping areas for the 2008 and 2013 multibeam surveys of Horseshoe Bend reveals that little or no large-scale morphological change occurred between the two surveys. Thus, the two datasets were merged with areas of overlap using the 2013 survey data only, thereby extending the spatial domain of bathymetric coverage throughout the loop. In contrast to Maier Bend, the bathymetric map produced for Horseshoe Bend shows only two pools: i) one along the inner bank upstream of the loop entrance (P1, Figure 8) and immediately downstream of a crevasse splay (CS), and ii) within the loop, a continuous pool along the outer bank that extends roughly the length of the point bar (P2, Figure 8). The outer bank pool (P2) displays abrupt upstream and downstream transitions and is continuous along the thalweg of the loop apex. However, the scour depth within the pool varies locally with the zone of deepest scour (~11 m below the top of the outer bank) located just upstream of the loop apex (Figure 8).

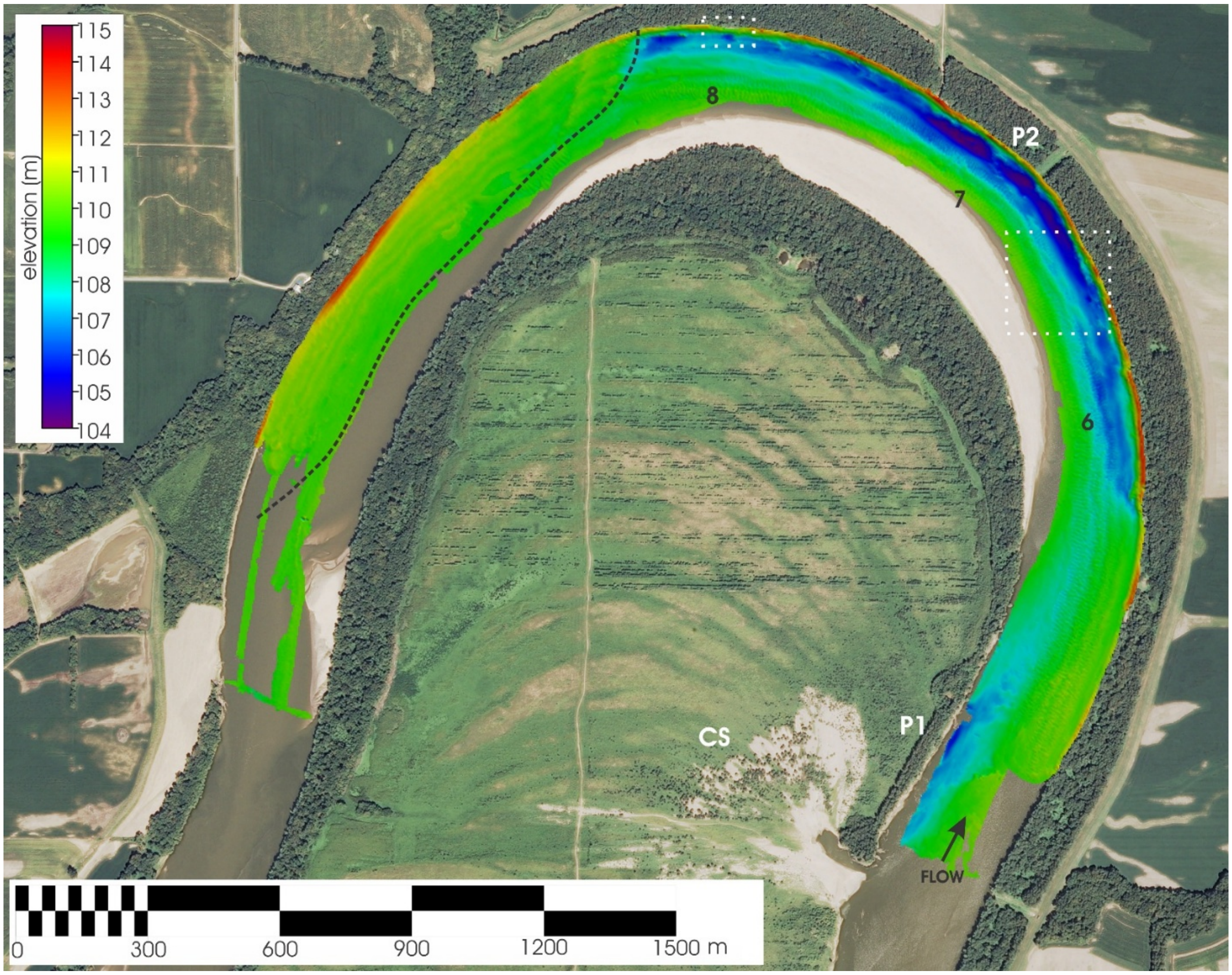

Figure 8: Bathymetric map derived from 2008 and 2013 multibeam surveys for Horseshoe Bend showing channel bed morphology. Arrow indicates flow direction, with a DEM resolution of 3 m. White dashed boxes indicate location of areas shown in Figures 9 and 10, and black dashed line approximates extent of bedrock outcrop within channel. Pools (P) and crevasse splay (CS) labeled.

Because flow conditions for the 2008 and 2013 MBES surveys were quite different, analysis of bedforms within Horseshoe Bend is restricted to areas encompassed by the 2013 survey. These bedforms primarily consist of two- and three-dimensional dunes that occur in the upstream limb of the loop, on the point bar, and along the inner bank of the downstream limb where bedrock is not exposed within the channel (Figures 8 and 9). In contrast to Maier Bend, no large (amplitude > 1 m) dunes are evident within the channel thalweg (Figure 9); however, both the 2008 and 2013 MBES surveys reveal a considerable amount of submerged large woody debris near the outer bank along the length of the pool (Figures 9 and 10).

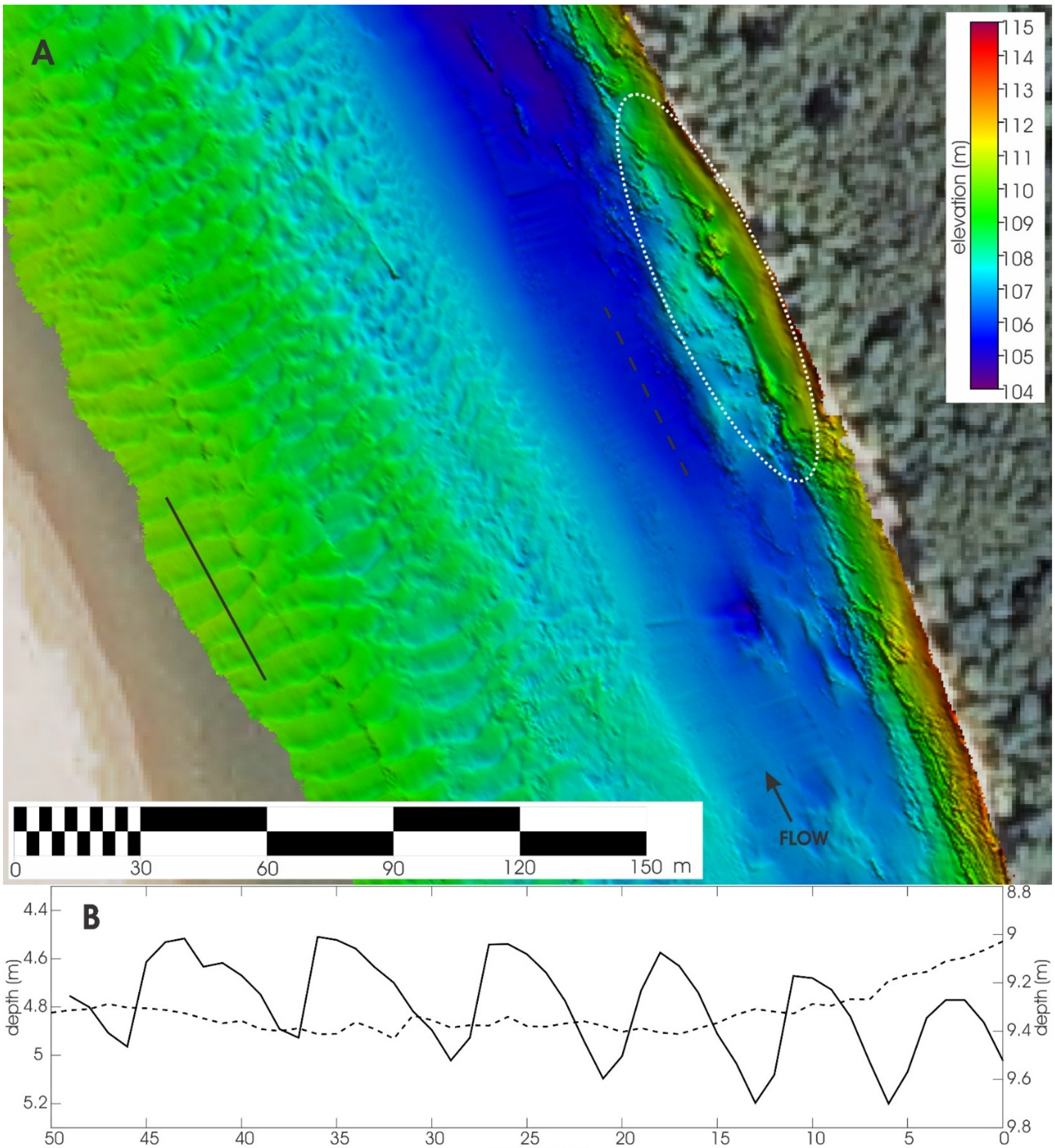

Figure 9: (A) Bathymetric map (0.5 m resolution) from 2013 MBES survey showing submerged large woody debris along the outer bank (dashed white oval) of Horseshoe Bend

(extent of area shown in Figure 8). (B) Profiles of bed topography along (solid line) point bar and (dashed line) thalweg (see part A for location of transects).

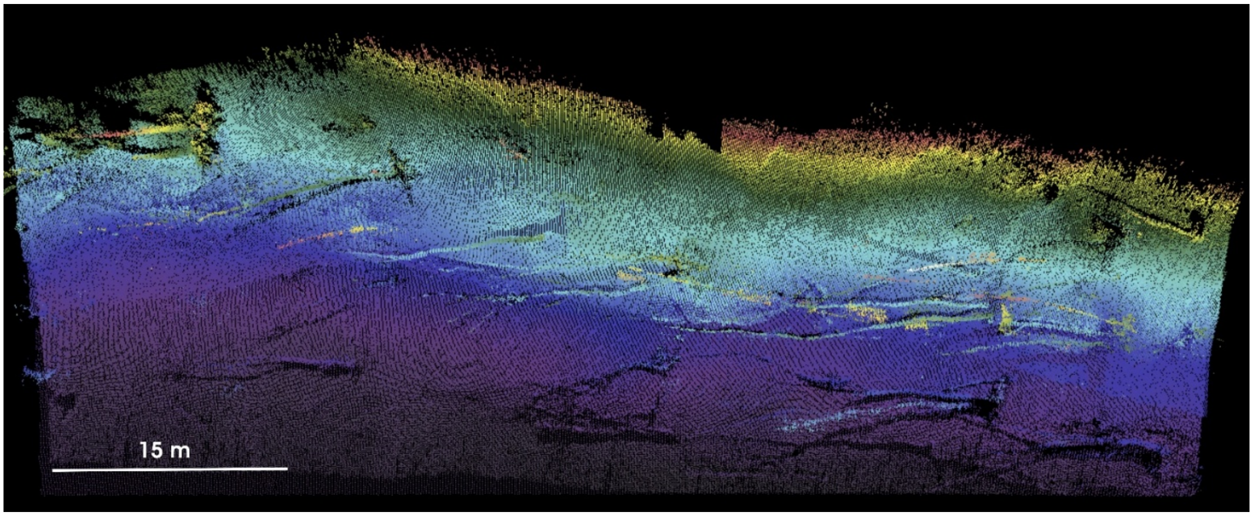

Figure 10: Bathymetric point cloud data from 2013 MBES survey showing submerged large woody debris along the outer bank of Horseshoe Bend. (Location of area shown in Figure 8).

4.3 Flow Characteristics

4.3.1. Maier Bend

The overall spatial pattern of depth-averaged velocity vectors at Maier Bend is similar for the two field campaigns. At the upstream limb (cross-sections 135-141), the cross-stream pattern of depth-averaged velocities is highly asymmetrical, with the highest velocities near the inner bank and the lowest velocities adjacent to the outer bank (Figure 11). As flow continues downstream into the apex region (cross-sections 146-151), the core of maximum velocity shifts towards the outer bank and the cross-stream pattern of depth-averaged velocity becomes asymmetrical, with the highest velocities along the outer bank and lowest velocities over the point bar. At the local outcrop of bedrock (cross-sections 152-153), the flow is deflected away from the outer bank, yet velocities along this bank remain high above the bedrock platform. Downstream of the bedrock (cross-sections 154-156), where the channel narrows, the depth-averaged velocities attain their highest values within the bend (>2 ms^{-1}). The zone of maximum velocity in this region becomes displaced away from the outer bank as the channel widens in the downstream direction (Figure 12). Inward-directed secondary velocity vectors clearly show that the bedrock platform and constriction immediately downstream (cross-sections 153 and 154, Fig. 13) deflects flow away from the outer bank. Downstream from the constriction (cross-section 155, Fig. 13) a strong gradient in streamwise velocities separates the core of maximum velocity (~2.25 ms^{-1}) from a zone of flow recirculation, which is defined by negative (upstream) streamwise velocities (-0.35 ms^{-1}). Outward-directed secondary velocity vectors occur along the outer bank where flow expands toward the flow separation zone downstream of the constriction (cross-section 156; Fig. 13).

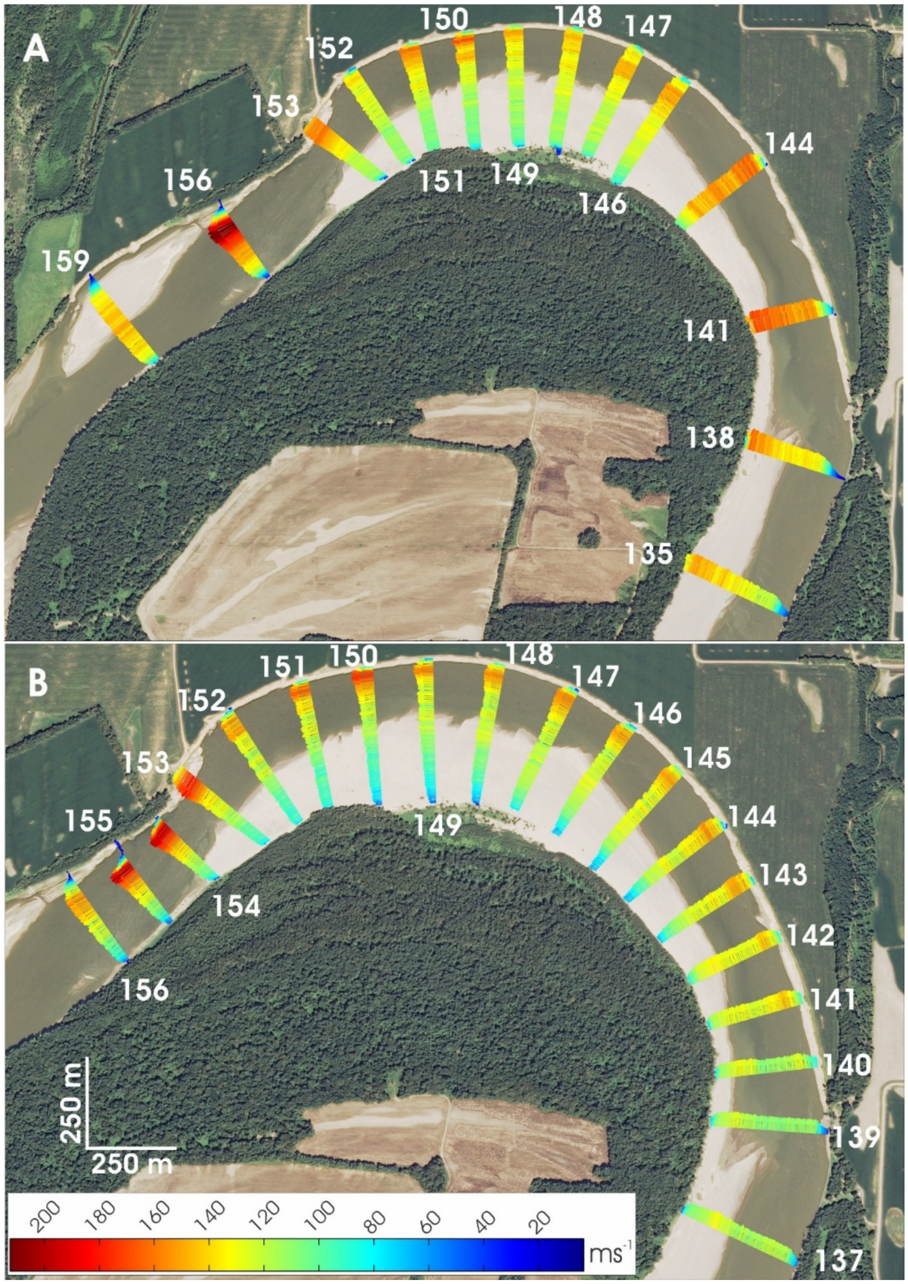

Figure 11: Depth-averaged velocity vectors along Maier Bend for (A) Campaign 1 (Q ~ 5,660 m^{3}s^{-1}), (B) Campaign 2 (Q ~ 2,450 m^{3}s^{-1}).

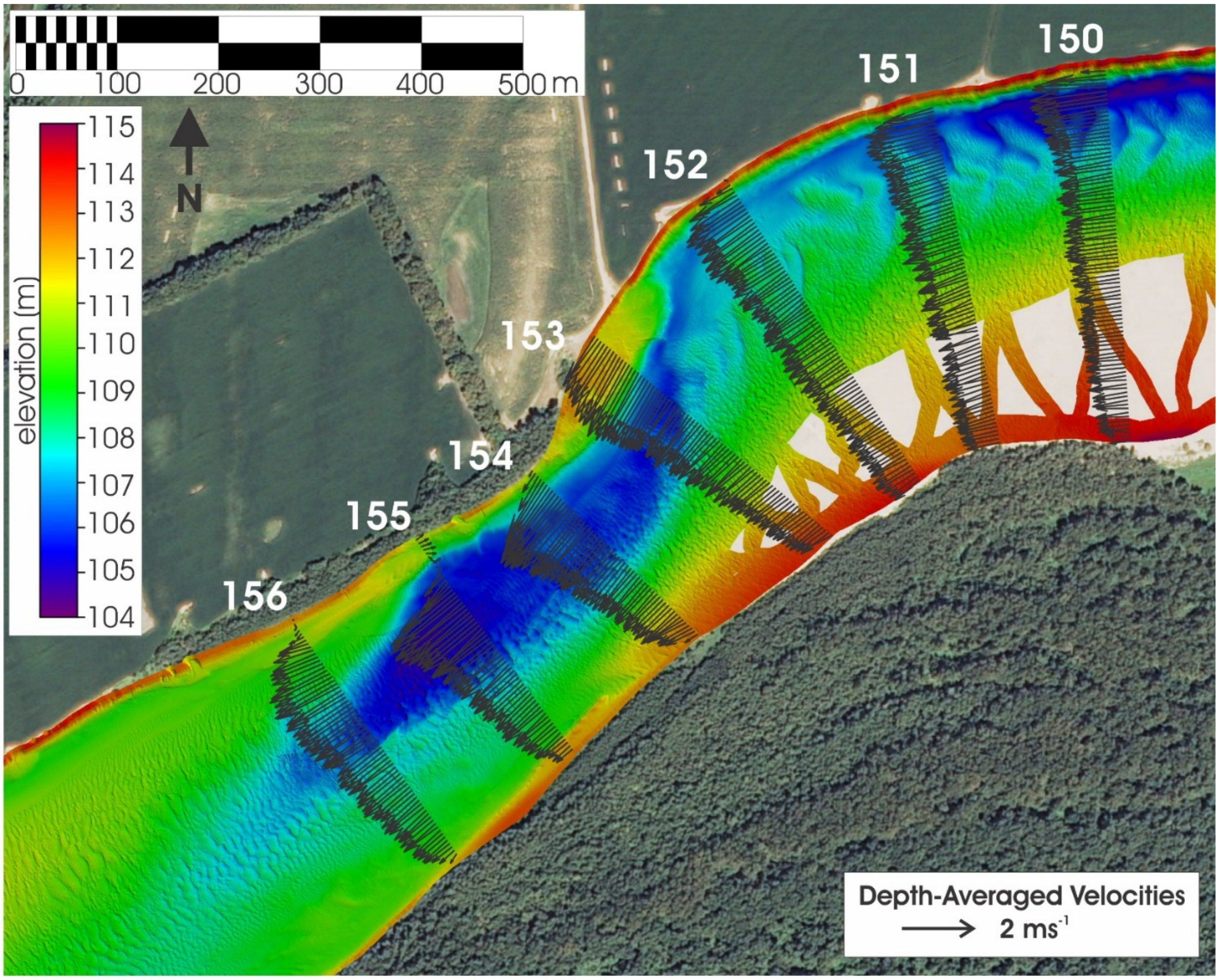

Figure 12: Depth-averaged velocity vectors (Campaign 2, Q ~ 2,450 m^3s^{-1}) shown with multibeam-derived channel morphology for Maier Bend. Note redirection of primary flow away from outer bank due to bedrock outcrop and the presence of a shear layer and zone of recirculation downstream of the bedrock.

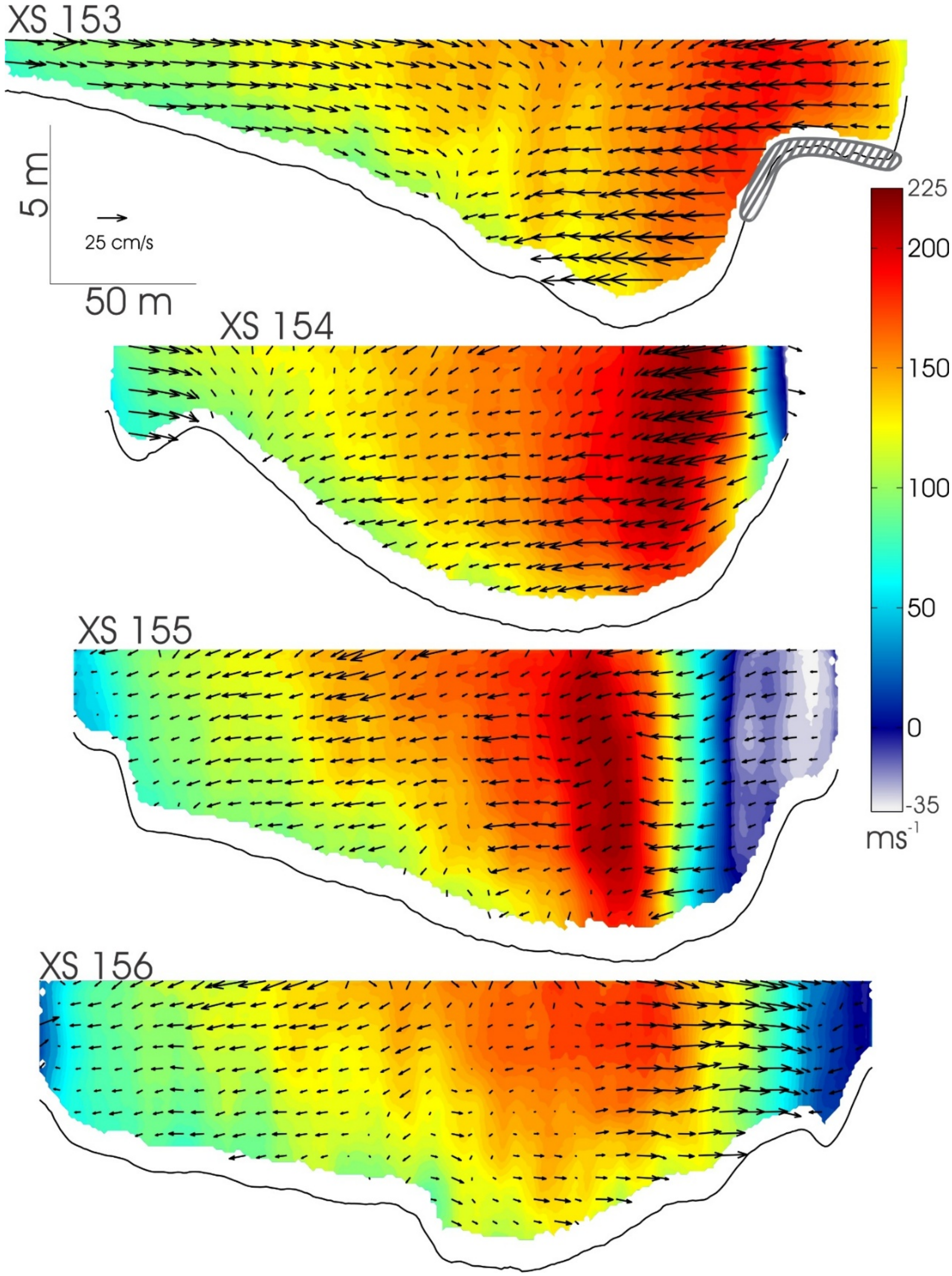

Figure 13. Cross-sectional flow fields at Maier Bend for June 2011 (Q ~ 2,450 m^3s^{-1}), using a cross section frame of reference showing streamwise (contours) and transverse (vectors) velocities. Cross-section 153 shows bedrock platform exposed within the channel (grey hatched region) directing flow away from the outer bank. Downstream of the bedrock flow separation occurs and a zone of recirculating fluid is present along the outer bank as shown by negative streamwise velocities.

Despite these overall similarities, flow characteristics differ slightly between Campaign 1 and Campaign 2. During Campaign 1, maximum velocities near the inner bank at the bend entrance are ~1.75 ms^{-1}, whereas during Campaign 2 the maximum velocities are about 25% less (~1.3 ms^{-1}) (Figure 11). During Campaign 2, the core of maximum velocity shifts to the outer bank immediately downstream of the bend entrance (cross-section 141, s = 4750 m), while during Campaign 1 this shift in the maximum-velocity core occurs farther downstream (cross-section 144, s = 5200 m, Fig. 11). As flow moves farther downstream (cross-sections 147-152, s = 5650-6400), the core of maximum velocity is located at a position about 80-85% of the cross-stream distance from the channel centerline toward the outer bank. The outward shift of the maximum-velocity core during both campaigns results in substantial deviation between the path of the cross-sectional median discharge (Q_{50}) and the channel centerline (Figure 14A). Within the upstream limb of the loop where the lateral extent of the point bar is limited, the path of Q_{50} is nearly identical to the channel centerline. However, within the loop, channel curvature increases and the lateral extent of the point bar expands. These increases in curvature and channel asymmetry through the bend redistribute mass and direct high-momentum flow toward the outer bank, resulting in an outward shift in the location of Q_{50}. The deviation between the path of Q_{50} and the channel centerline reaches a maximum near the loop apex. The outward shift in Q_{50} is slightly greater in Campaign 2 (~110 m from centerline), the near-bankfull flow, than in Campaign 1 (~90 m from centerline), the overbank flow. Downstream of the loop apex the flow encounters the bedrock platform and is redirected away from the outer bank, reducing the deviation between the path of Q_{50} and the channel centerline (Figure 14A).

Cross-sectional velocity fields and patterns of secondary velocity vectors show the differences between the two campaigns and advection of the maximum velocity core toward the outer bank (Figure 15). As flow travels through the upstream portion of the bend (cross section 144-146), channel width increases and the cross-sectional distribution of velocity becomes more asymmetric as the point bar influences channel shape (Fig. 15). During Campaign 1, flow in this upstream part of the bend is directed outward within the thalweg and inward over the point bar, suggesting flow divergence. However, during Campaign 2, a decrease in flow stage results in relatively shallow flow over the top of the point bar, confinement of most flow within the thalweg, and enhanced topographic steering of the flow toward the outer bank (Fig. 15). Immediately downstream of the bend apex (cross section 149), secondary velocity vectors near the surface are directed outward, whereas those near the bed are directed inward, indicating the development of helical motion (Fig. 15). The cross-sectional velocity fields also show that the core of high velocity adjacent to the outer bank extends from near the surface to the bank toe, with velocity magnitudes being slightly larger during Campaign 2 (~1.85 ms^{-1}) than Campaign 1 (~1.75 ms^{-1}).

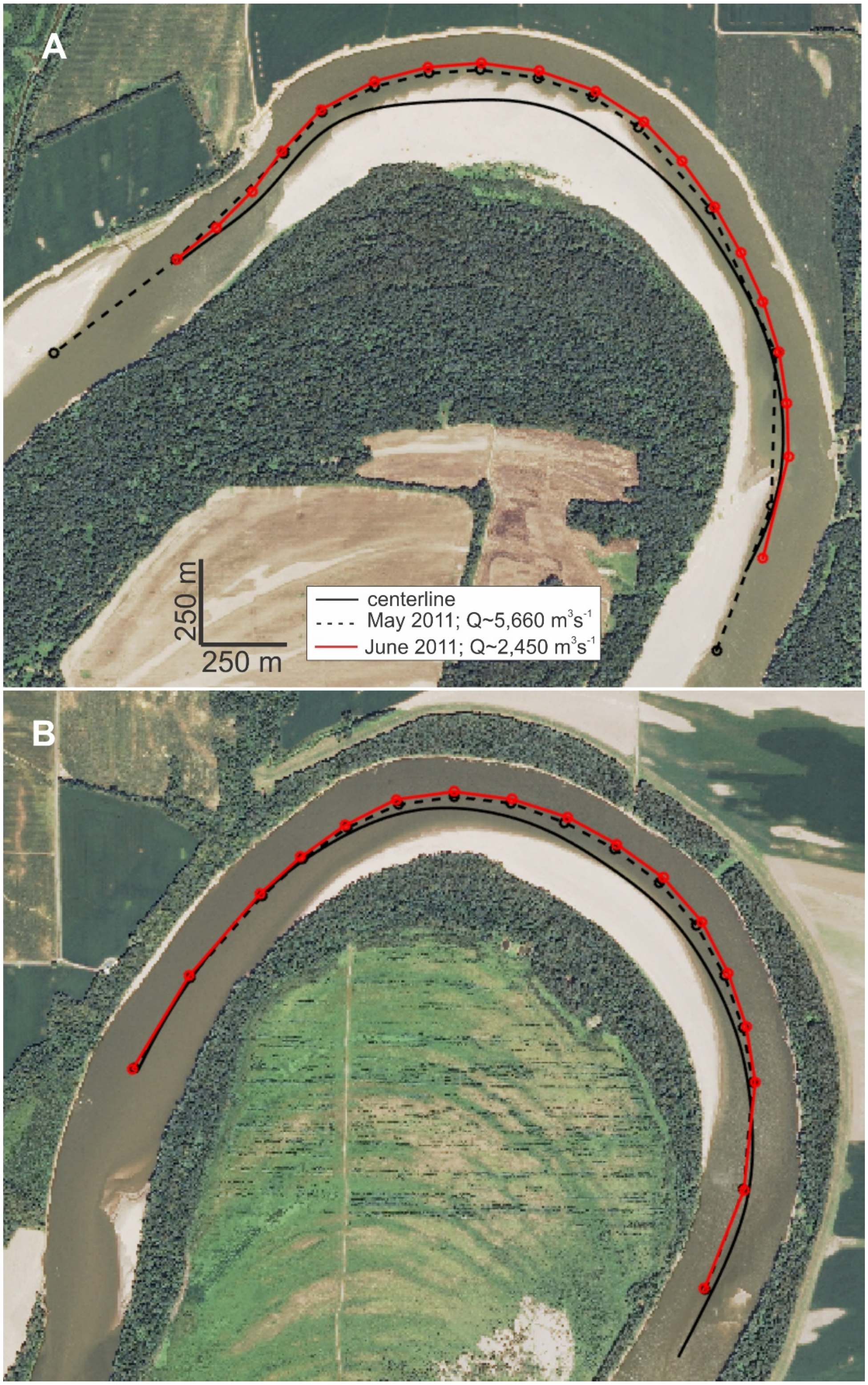

Figure 14: Path of cross-sectional median discharge (Q_{50}) through (A) Maier Bend and (B) Horseshoe Bend for Campaigns 1 (Q ~ 5,660 m3s-1) and 2 (Q ~ 2,450 m3s-1), shown with the channel centerline calculated from banklines.

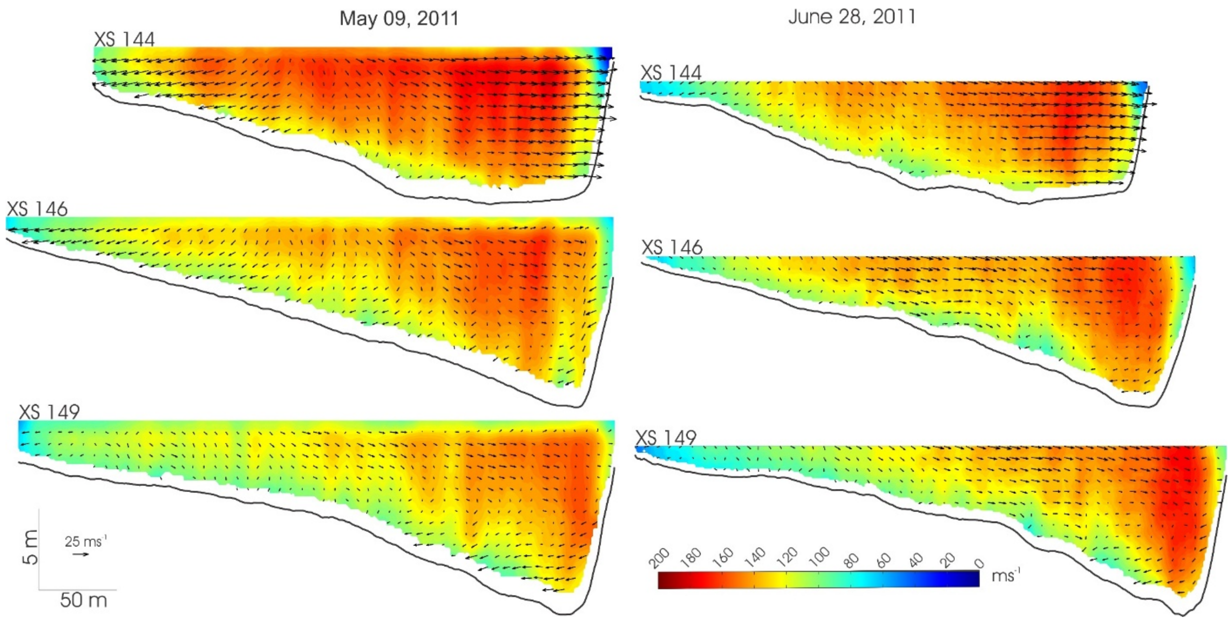

Figure 15: Cross-sectional flow fields at Maier Bend for May (*Q* ~ 5,660 m^3s^{-1}) and June 2011 (*Q* ~ 2,450 m^3s^{-1}), using a cross section frame of reference showing streamwise (contours) and transverse (vectors) velocities.

4.3.2. Horseshoe Bend

At the entrance to Horseshoe Bend, the highest velocities (~1.75 ms^{-1}) are located near the inner bank, whereas velocities adjacent to the outer bank are $\leq$ 0.05 ms^{-1} (Fig. 16). Compared to Maier Bend, the outward shift of maximum velocities within Horseshoe Bend is less prominent. For both campaigns, a gradual outward shift in maximum velocities in the upstream part of the bend (cross sections 65-68, s = 2550-3000) results in a broad zone of fairly uniform velocities within the center of the channel. In campaign 1, a distinct core of maximum velocity near the bend apex is not clearly visible from the pattern of depth-averaged vectors (Fig. 16), but examination of the velocity data indicates that the greatest outward shift of the maximum velocity core occurs at the downstream part of the apex region (cross-sections 70-71, s = 3300-3450), where this core is located about 75% of the cross-stream distance from the channel centerline to the outer bank. In Campaign 2, the core of maximum velocities near the apex is somewhat more distinct

(Fig. 16) and this core is located closest to the outer bank (80% of the cross-stream distance from the centerline to the outer bank) at the same location as in Campaign 1 (cross-sections 70-71, s = 3300-3450). Within the downstream limb of the bend (cross sections 75-80), the bedrock outcrop along the outer bank constricts the channel width, accelerating the flow and producing the highest velocities within the reach; however, the core of maximum velocity is shifted away from the outer bank relative to its position farther upstream. At many locations in Horseshoe Bend, velocities immediately adjacent to the outer bank are relatively small (0.10 – 0.75 ms^{-1}) (Fig. 17). Cross-sectional velocity fields near the bend apex (cross sections 68-70) reveal that the zone of near-bank reduced velocity extends to the bank toe, and, despite velocity magnitudes as high as ~1.8 ms^{-1} during Campaign 2 (roughly 20% higher than Campaign 1), the zone of reduced velocity near the outer bank persists. The orientations of secondary velocity vectors are outward near the surface and inward near the bed, suggesting that helical motion has developed through the bend (Fig. 17). However, this pattern of fluid motion is present only over the point bar and thalweg; near the outer bank the extent of helical motion is restricted by the zone of reduced velocity.

The spatial pattern of flow through Horseshoe Bend shows a similar shift in the path of Q_{50} from the channel centerline to that observed for Maier Bend; however, compared to Maier Bend, the locus of maximum deviation between the centerline and path of Q_{50} at Horseshoe Bend is shifted upstream (Figure 14). Near the loop entrance, where channel curvature and the lateral extent of the point bar are limited, the path of Q_{50} follows the centerline closely (Figure 14B). As flow moves into the bend, increasing channel curvature and topographic steering of the flow by the expanding point bar along the inner bank shifts the zone of maximum streamwise velocities toward the outer bank. The greatest difference (~65 m) between the location of the centerline and the position of Q_{50} for Campaign 2 occurs near the loop apex. Deviation between the path of Q_{50}

and the centerline decreases toward the downstream end of the loop, becoming nearly coincident at the tail of the point bar (Figure 14B).

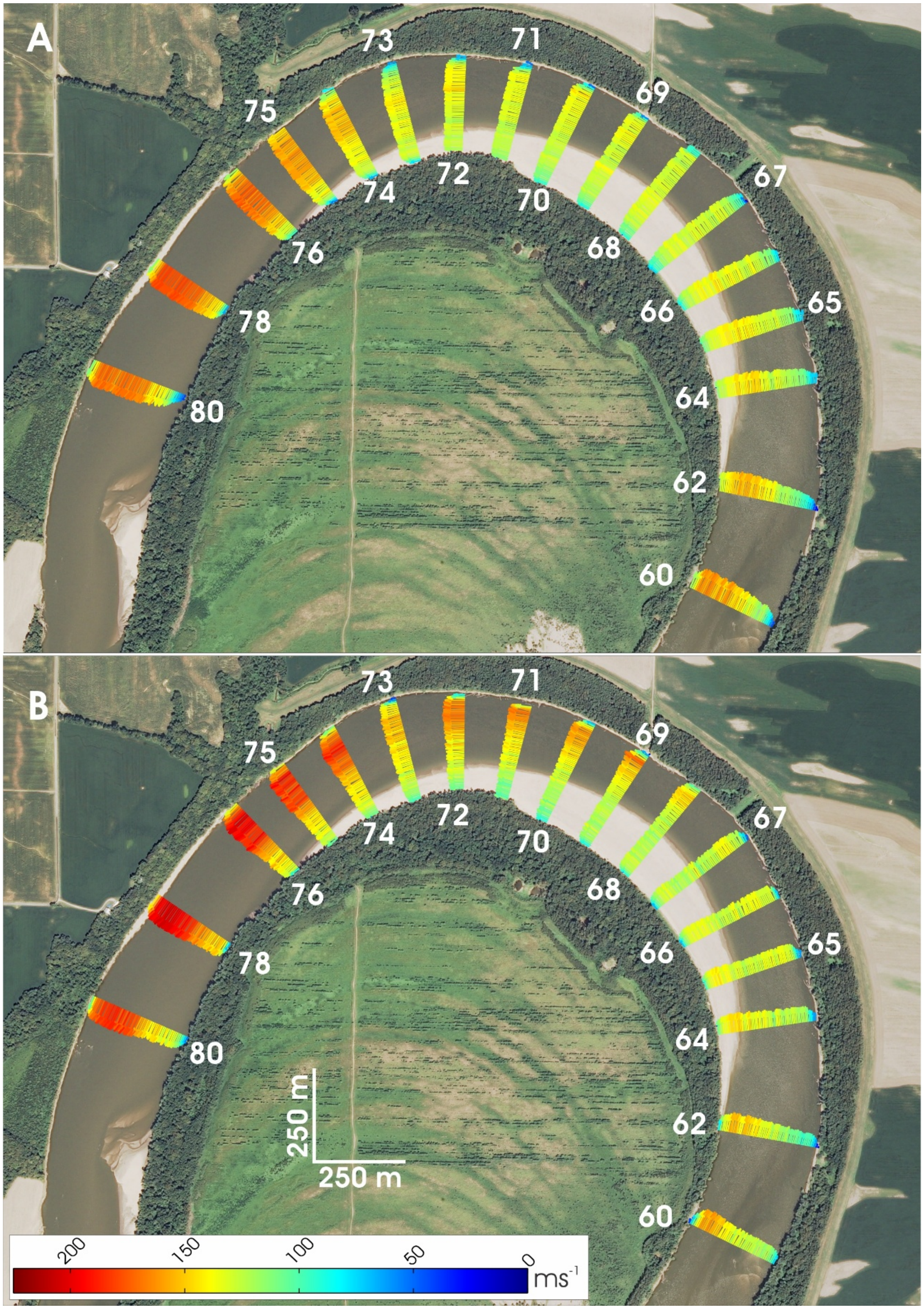

Figure 16. Depth-averaged velocity vectors at Horseshoe Bend for (A) Campaign 1 (*Q* ~ 5,660 m3s-1) and (B) Campaign 2 (*Q* ~ 2,450 m3s-1).

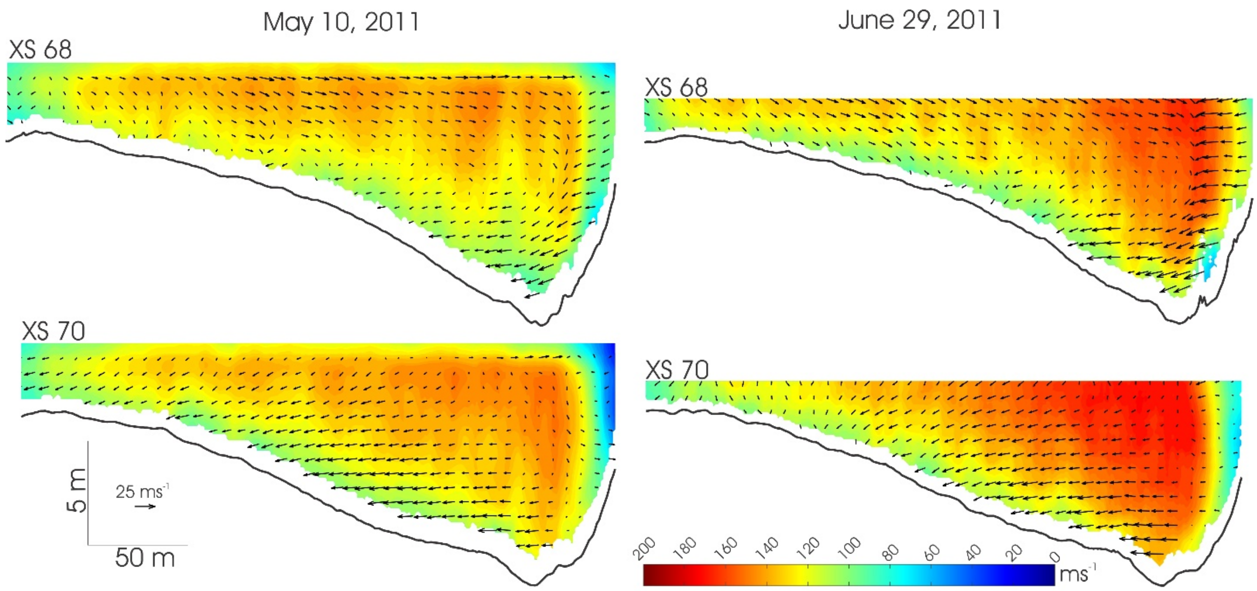

Figure 17: Cross-sectional flow fields at Horseshoe Bend for May (*Q* ~ 5,660 m3s-1) and June 2011 (*Q* ~ 2,450 m3s-1), using a cross section frame of reference showing streamwise (contours) and transverse (vectors) velocities.

4.3.3. Mass and momentum redistribution

The spatial patterns of Q_{50} (Figure 14) indicate that the flow path deviates from the path of the channel centerline in both loops. To further explore this phenomenon, the spatial position of the median cross-sectional unit discharge $U_s h$ can be examined to show how changes in the spatial position of median depth (h) and median velocity (U_s) contribute to the redistribution of mass through each loop (e.g. Blanckaert, 2010). This method involves plotting the transverse positions (n coordinates) of the median unit discharge $U_s h$, median flow depth h, and median depth-averaged streamwise velocity U_s against streamwise distance along the channel centerline (s) (Figures 18A-D). These plots reveal close agreement between the spatial pattern of $U_s h$ and h for both loops and for each date of measurement (Figures 18 A-D). This result suggests that mass redistribution of the flow through the loops is strongly influenced by the changing depth distribution across the channel, reflecting topographic steering by the point bar. The spatial pattern of U_s generally follows a similar trend to $U_s h$ and h, but maintains transverse positions closer to the channel centerline. Moreover, at Horseshoe Bend during Campaign 2, the median streamwise velocity shifts laterally in a different pattern than $U_s h$ and h (Figure 18D). Additionally, at streamwise distances greater than ~3700 m at Horseshoe Bend, the pattern of U_s becomes aligned with the pattern of $U_s h$ more closely than does the pattern of h (Figures 18C-D), which most likely reflects the influence of extensive bedrock exposed within the downstream limb of the loop. Thus, the spatial pattern of mass flux ($U_s h$) is also influenced to some extent by the redistribution of momentum (U_s) within the loop.

Quantitative analysis of the redistribution of U_s within meanders bends should be based on the depth-averaged streamwise momentum equation (Dietrich and Smith, 1983; Blackaert, 2010). Such an analysis requires accurate data on streamwise water surface gradients, which are not available in the present study. If it is assumed that the streamwise water surface gradient through a bend is fairly constant, major factors contributing to the redistribution of streamwise momentum include topographic steering, which is related to changes in depth, and helical motion, which is related to channel curvature. A key factor influencing channel migration is the extent to which redistribution of momentum affects near-bank velocities. The magnitude of near-bank velocities has been linked to rates of channel migration (Pizzuto and Meckelnburg, 1989) and is included in convolution models that define channel migration as a spatially weighted function of upstream channel curvature (Parker and Andrews, 1986; Guneralp and Rhoads, 2010).

In the absence of water-surface gradient data, the extent to which redistribution of mass and momentum affects depth-averaged velocities near the outer bank is examined by plotting values of U_{80}, $h_{n=-100}$, and C_c versus s for the two flows in each meander loop (Figure 18E-H). Here, U_{80} is the depth-averaged streamwise velocity at a location corresponding to 80% of the transverse distance from the channel centerline to the outer bank, $h_{n-=-100}$ is the channel depth at a transverse distance of 100 m from the centerline toward the inner bank, and C_c is the cumulative curvature along the channel centerline from the bend entrance to a particular location. Within the upstream limb of each loop, for each field campaign U_{80} increases rapidly as $h_{n=-100}$ abruptly decreases and C_c increases (Figures 18E-H, shaded regions). Downstream of this zone of pronounced increase in near-bank velocity, both $h_{n-=-100}$ and U_{80} remain fairly constant at Maier Bend even though C_c continues to increase linearly (Figures 18E-F). At the downstream end of the loop, U_{80} decreases as flow expands beyond the region of bedrock and a region of separation develops along the outer bank. At Horseshoe Bend, beyond of the zone of increase in near-bank velocity, U_{80} fluctuates, but does not increase systematically, while $h_{n-=-100}$ systematically increases. Toward the downstream end of the reach, where bedrock is exposed along the outer bank, U_{80} locally increases. Cumulative curvature increases systematically until reaching the inflection point at the downstream end of the loop.

The patterns of U_{80}, $h_{n=-100}$, C_c suggest that at the upstream end of the two loops both topographic steering associated with decreasing depth along the inner bank as well as outward transport of momentum associated with channel curvature lead to an abrupt increase in near-bank velocities. Once this momentum transfer at the upstream end of the loop occurs, the continued curvature of the channel sustains, but does not greatly enhance, the magnitude of near-bank velocities. The near-bank velocity data also clearly indicate that values of U_{80} are greater at near-bankfull flow in both loops (Campaign 2) compared to values for overbank flow (Campaign 2) (Figure 18; Table 2).

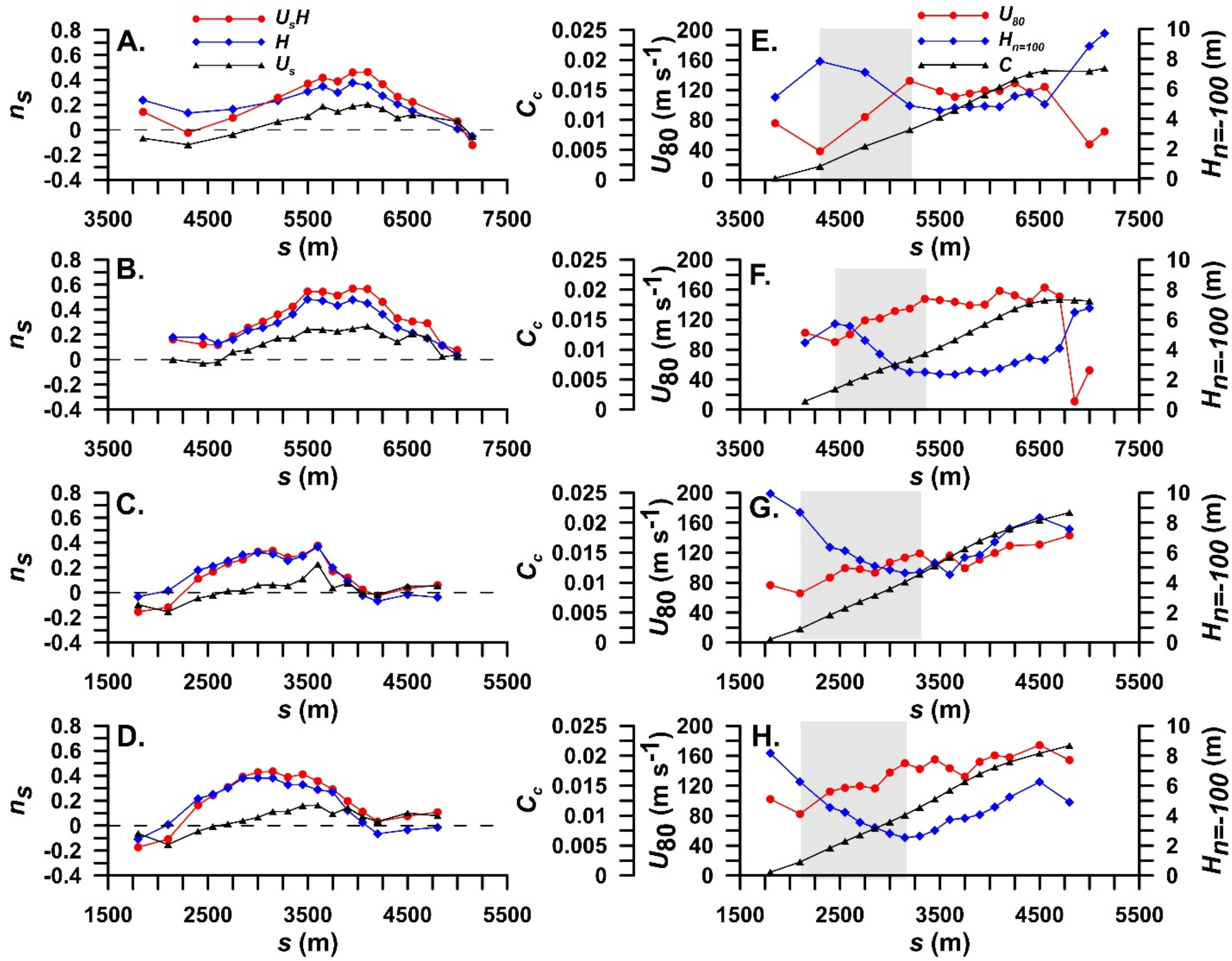

Figure 18: A-D) Normalized transverse position of cross-sectional median unit discharge $U_s h$, median flow depth h, and median depth-averaged streamwise velocity U_s around each loop. E-H) Spatial evolution of U_{80}, $h_{n=-100}$, and C. Data presented for Maier Bend, Campaign 1 (A and E); Maier Bend, Campaign 2 (B and F); Horseshoe Bend, Campaign 1 (C and G); Horseshoe Bend, Campaign 2 (D and H).

Although the redistribution of mass and momentum appears to be broadly similar throughout the two loops, the pattern of near-bank depth-averaged velocity vectors around Horseshoe Bend shows a pronounced region of reduced velocities that is not present around Maier Bend. To evaluate this difference quantitatively, statistical comparisons were conducted of U_{80} and U_{95} for the two bends, where U_{95} is the depth-averaged velocity at 95% of the channel half-width distance from the centerline to the outer bank, i.e. the velocity magnitude very close to the outer bank. Only cross-sections upstream of the bedrock sections of the two bends were included in the statistical comparison to eliminate the effect of bedrock on near-bank flow. Results show that the ratio of the mean values of U_{95} and U_{80} is much less for Horseshoe Bend than for Maier Bend, indicating that depth-averaged velocity magnitudes decrease to a greater extent near the outer bank at Horseshoe Bend than at Maier Bend (Table 2). Moreover, the ratio of coefficients of variability for U_{95} and U_{80} is greater at Horseshoe Bend than at Maier Bend, demonstrating that depth-averaged velocities near the bank at Horseshoe Bend are more variable than those at Maier Bend. Given that both loops exhibit similar patterns of mass and momentum redistribution, the likely factor contributing to reduced velocity along the outer bank of Horseshoe Bend is the presence of abundant LWD. The differences in the near-bank streamwise velocities confirm indicate a stronger effect of roughness on the flow near the outer bank at Horseshoe Bend than at Maier Bend, which lacks near-bank LWD.

Table 2: Statistics of near-bank depth-averaged streamwise velocities at 80% and 95% of the channel half-width upstream of bedrock influence.

	Date	μ_{80}	μ_{95}	σ_{80}	σ_{95}	c_{v80}	c_{v95}	μ_{95}/μ_{80}	c_{v95}/c_{v95}
Maier Bend	5/9/2011	110.0	74.7	26.9	31.9	0.25	0.43	0.68	1.75
	6/28/2011	133.5	86.9	19.6	18.7	0.15	0.22	0.65	1.47
Horseshoe Bend	5/10/2011	100.1	54.0	15.1	17.9	0.15	0.33	0.54	2.21
	6/29/2011	128.2	68.6	21.1	30.8	0.16	0.45	0.54	2.73

5 Discussion

The results from this study provide insight into spatial patterns of three-dimensional flow structure and bed morphology in large elongate meander loops, how these patterns vary under different discharge conditions, and the influence of differences in outer bank roughness characteristics on these patterns. Generally, the patterns of three-dimensional flow structure within the elongate meander loops examined in the present study are in agreement with previous laboratory and field investigations of flow structure through high amplitude, elongate meander bends (Jackson, 1975a,b; Whiting and Dietrich, 1993a,b; Frothingham and Rhoads, 2003; Abad and Garcia, 2009a,b; Blanckaert, 2010; Termini and Piraino, 2011; Engel and Rhoads, 2012). At the upstream limb of the loops, the highest velocities are located along the inner bank, reflecting both inherited flow structure from the upstream bend of opposite curvature (Jackson, 1975a; Abad and Garcia, 2009a), as well as spatial variations in water-surface topography through sequential bends of opposing curvature that lead to high velocities along the inner bank at bend entrances (Dietrich, 1987). As flow moves through the bends, topographic steering of the flow by the point bar along with centrifugal effects associated with flow curvature shift the core of maximum velocity from the inner to the outer bank (Figures 11, 16, and 18). Upstream of the bend apex, the discharge vector is oriented toward the outer bank relative to the orientation of the channel centerline, resulting in a net increase in discharge over the outer half of the channel. This net outward movement of flow can be attributed mainly to topographic steering by the point bar, which diminishes the cross-sectional area over the inner portion of the channel (Figure 18). Near the bend apex, secondary velocity vectors in both loops display outward directed near-surface flow and inward directed near-bed flow – a pattern indicative of large-scale curvature-induced helical motion. This helical motion advects high-momentum, near-surface flow toward the outer bank, maintaining large near-bank velocities and boundary shear stresses in the channel thalweg. At both bends, the core of maximum velocity is positioned closest to the outer bank immediately downstream of the loop apex, consistent with findings of previous field and laboratory studies (Jackson, 1975a,b; Whiting and Dietrich, 1993a; Frothingham and Rhoads, 2003).

As illustrated by the results for Horseshoe Bend, the presence of large woody debris (LWD) along the outer bank can produce substantial differences in the overall flow structure through the bend compared to patterns of flow in meandering channels that lack large wood (e.g. Maier Bend).

In particular, as curvature and the effect of topographic steering increase through the loop and the core of maximum velocity gradually shifts toward the outer bank (Figure 18), the increased flow resistance generated by submerged trees leads to the development of a zone of low velocities adjacent to the outer bank (Figures 16-17). As a result, the magnitude of streamwise velocities in the vicinity of the outer bank are diminished to a greater extent than near-bank velocities in loops without abundant near-bank LWD (e.g. Maier Bend, Figure 15 and Table 2). Moreover, the presence of LWD inhibits extension of large-scale curvature-induced helical motion into the near-bank region. These findings are generally consistent with past work on flow structure in a small meander bend with woody vegetation along the outer bank (Thorne and Furbish, 1995).

The present study has also documented the effect of variable high discharges on the flow structure through elongate bends. For the near-bankfull conditions at Maier Bend (Campaign 2), the shift of maximum velocity from inner to outer bank occurred at a location roughly coincident with the intersection of the inner bank tangent with the outer bank, a finding consistent with experimental results (Whiting and Dietrich, 1993a,b). However, for overbank conditions (Campaign 1), the core of maximum velocity crossed from inner to outer bank farther downstream, close to the bend apex (Figure 11). This lag in the shift of the maximum velocity core is most likely related to the diminished topographic steering caused by the point bar during this overbank event given that a large proportion of the total flow moved across the interior part of the meander loop in the down-valley direction. However, it is interesting to note that near-bank velocities in the upstream part of the bend increase abruptly at nearly the same position in the loop during both events (Figure 18E-F). Because near-bank velocities influence outer bank erosion rates, the effect of mass or momentum redistribution on these velocities is important for understanding patterns of bank erosion and channel migration. This zone where near-bank velocities increase abruptly corresponds closely with the location where bank erosion within Maier Bend begins (Konsoer et al., 2016). Maximum rates of bank erosion occur farther downstream near the bend apex where the maximum velocity core is closest to the outer bank. During the overbank event, near-bank velocities near the bend apex are less than velocities at this location during the near-bankfull event.. In addition to the diminished topographic steering effect during the overbank flow, this reduction in near-bank velocities may be partly related to *flow bypass* (Jackson, 1975a, p. 38), whereby overbank flow extracts momentum from the flow in the main channel, resulting either in steady or decreasing depth-averaged velocities as discharge increases from bankfull to overbank conditions.

Similarly, at Horseshoe Bend depth-averaged, near-bank velocities during the near-bankfull event are greater than those during the overbank event (Figure 16). However, in contrast to Maier Bend, the position of the core of maximum velocity throughout the loop does not appear to be strongly influenced by the change in flow conditions. Instead, the position of the core of maximum velocity remains relatively farther from the outer bank for both campaigns than at Maier Bend. The abundant LWD along this bank is effective at preventing penetration of high momentum fluid, which can produce high boundary shear stresses, into the near-bank region during geomorphically active flood events. Additionally, given that the curvature series for Maier and Horseshoe bends display similar peak magnitudes and both bends contain large point bars capable of steering flow toward the outer bank, the LWD along the outer bank at Horseshoe Bend may partly contribute to differences in the deviation of the path of Q_{50} from the channel centerline. At Maier Bend, the path of Q_{50} reaches a maximum deviation near the apex of ~110m, roughly 55% of the distance from the centerline to the outer bank, whereas at Horseshoe Bend the outward shift of Q_{50} is only ~65 m, roughly 40% of the distance from the centerline to the outer bank.

At Maier Bend, the largest outer bank pool upstream of the loop apex (P3) is located close to the region where the core of maximum velocity intersects the outer bank (Figures 5 and 11), a finding similar to that of past experimental studies (Whiting and Dietrich, 1993a,b; Termini 2009), and findings from small elongate meander loops (Engel and Rhoads, 2012). Additionally, the locations of the pools along the outer bank upstream of the bedrock outcrop appear to be closely correlated to local maxima within the curvature series. For example, the location of P3 corresponds closely with the first local maxima in the curvature series for Maier Bend (i.e. Figures 4-5, #1), whereas P4 is broadly centered around the maximum curvature value (i.e. Figure 4-5, #3), with the deepest scour occurring immediately downstream of the locus of peak curvature. The local topographic high along the outer bank between these two pools occurs near a local minimum in the curvature series (i.e. Figures 4-5, #2). This finding is also consistent with results of previous studies, which have shown that the locations of multiple pools in elongate bends are associated with spatial variations in channel curvature (Harvey and Hooke, 1983; Engel and Rhoads, 2012).

In contrast to Maier Bend, only one large, continuous pool at Horseshoe Bend is present along the outer bank. Although the upstream and downstream extents of the pool coincide roughly with the two local maxima of the curvature series (i.e. Figure 4 and 8, #6 and #8), the local minima in curvature (#7) does not correspond to a local topographic high along the outer bank, but in fact at this location the depth of the outer bank pool reaches its maximum. Modification of the near-bank flow by abundant LWD may disrupt the relationship between channel curvature and pool development.

Despite the presence of multiple outer bank pools along Maier Bend, the bed topography throughout this elongate meander loop does not appear to be organized into a series of shingle bars (i.e. Whiting and Dietrich, 1993a, b). Likewise, the bed topography of Horseshoe Bend does not show evidence of overlapping, channel-wide, bar forms throughout the loop. The point bars in the two elongate meander loops are not segmented into discrete lobes with distinct bar fronts. Instead, the bed morphology is better characterized as possessing a single point bar that extends over much of the length of the inner bank, two or more pools associated with maxima in channel curvature, migrating dunes that scale with flow depth, and zones of scour along the outer bank that are influenced by bedrock outcrops and large woody debris. The reason why the meander loops in the Wabash River lack well-defined shingle bars is unclear, but previous field studies have confirmed that such bars also are absent in compound meander loops (Engel and Rhoads, 2012). Possible factors that could account for this discrepancy between results of laboratory and field studies include scaling issues related to flow width:depth ratios and to bed material characteristics, or to the effects of flow unsteadiness on bar development. Further work is needed to evaluate the utility of the shingle-bar concept in meandering rivers.

Spatial variation in bedform morphology throughout these two elongate meander loops is dependent on the local hydraulic conditions, which are influenced by channel curvature, flow discharge, and the presence of bedrock outcrops and in-channel wood. Within the upstream limb of Maier Bend, channel curvature values are small, depth-averaged velocities are asymmetric with highest values along the inner bank, and the strength and coherence of secondary flow is weak. In this reach, bedform morphology changes across the channel from two-dimensional dunes along the outer bank, to smaller dunes in the middle of the channel, to a barchan dune field migrating over a gravel-covered bar along the inner bank. The barchan dune field demonstrates that sand supply is locally limited over the gravel bar. Similarly, exposed bedrock within the downstream limbs of these meander loops decreases the channel width, which in turn accelerates the flow. The increased velocities lead to local scour of the channel bed where the substrate is mobile (e.g. Maier

Bend) or, where alluvial cover is thin or absent, exposure of bedrock on the bed of the channel (e.g. Horseshoe Bend). Thus, bedforms are absent near the bedrock at these locations.

Dune wavelengths and amplitudes obtained from the high-resolution multibeam bathymetry for both meander loops do not always agree with predictions of dune geometries based on empirical relations. Using measurements of flow depth and a characteristic median grain size d_{50} for bed material of 0.0007 m, bedform geometries for the Wabash River (Figures 6, 7 and 9) were compared to predictions based on: $\lambda = 6.25h$ and $\Delta = 2.5h^{0.7}d_{50}^{0.3}$, where λ is dune wavelength, and Δ is dune amplitude (Julien and Klaassen, 1995). Predicted dune wavelengths generally are 3-7 times larger than measured values, while predicted amplitudes are roughly 1.5 times larger than measured values. However, predicted values of dune wavelength (59 m) and amplitude (1.4 m) do correspond closely to measured values of wavelength (50 m) and amplitude (1.5 m) of the large composite dunes located immediately downstream of the loop apex on Maier Bend. Despite this local agreement, it is worth noting that immediately upstream of the apex on Maier Bend the average dune wavelengths (17 m) and amplitudes (1.2 m) are much smaller, and the transition between small dunes and large composite dunes in the apex region is rather abrupt (Figure 7). The lack of agreement between the observed and predicted bedform geometries might indicate that bedform morphology was not in equilibrium with local hydraulic conditions and was adjusting to unsteady flow conditions related to the passing flood wave..

Lastly, mesoscale bedform development within these two bends may be influenced by the presence or absence of large woody debris. At Maier Bend, where LWD along the outer bank is absent, large dunes develop in the thalweg immediately adjacent to the outer bank. In contrast, at Horseshoe Bend, where abundant LWD strongly affects hydraulic conditions, large dunes are not present in the thalweg. The hydraulic effects of the LWD at Horseshoe Bend may sufficiently disrupt patterns of sediment transport to inhibit the development of dunes within the channel thalweg.

6 Conclusions

The present paper has examined spatial patterns of three-dimensional flow structure and bed morphology within two elongate meander loops on a large meandering river during two flow events with different discharges. The two bends have similar planforms and are influenced locally by outcrops of bedrock, but have different outer-bank roughness characteristics. The principal findings are:

1. In large elongate loops , the highest velocities are observed along the inner bank at the bend entrance with the zone of maximum velocity crossing over to the outer bank upstream of the loop apex. Redistribution of mass and momentum is dependent on flow stage with greater redistribution towards the outer bank occurring during near-bankfull events than during overbank events. As a result, near-bank velocities are greater during near-bankfull flow than during overbank flow. Redistribution of mass and momentum around the loop appears to be primarily effected by topographic steering of the flow by the point bar with momentum redistribution by curvature effects sustaining high near-bank velocities in downstream parts of the loops.
2. In elongate meander loops with abundant near-bank large woody debris, a zone of low flow velocity is produced near the outer bank that persists along the majority of the bend. This zone of low velocity is situated adjacent to the maximum core of velocity within the channel thalweg and confines curvature-induced helical motion to the region between the channel thalweg and the face of the point bar. In addition to enhancing the lateral gradient

in depth-averaged near-bank velocities, this LWD also increases the lateral gradient in relatively variability of near-bank velocities.

3. Channel bed topography in the loop without LWD displays multiple outer bank pools, whereas bed topography in the loop with LWD exhibits only one large, outer bank pool that extends the length of the point bar. The morphology of these bed features does not conform to the structure of shingle bars that develop in experimental channels, but the location and size of the pools in the Wabash River are related to spatial variations in channel curvature and three-dimensional flow structure through the loops. Observed bedform morphology also was not consistent with morphology predicted by empirical relationships based on flow depth and grain size..

Although time-averaged measurements of three-dimensional velocities and bed morphology were obtained herein for two different high discharge flow events, future research should examine a wider range of geomorphically relevant discharge events to investigate the temporal response of the bed morphology to hydraulic conditions throughout elongate meander loops. Furthermore, detailed investigations of the interactions between outer bank roughness, near-bank three-dimensional flow structure, and rates of bank erosion and migration should be conducted to explore the efficacy of LWD, slump blocks, and topographic roughness on mitigating planform evolution in large rivers.

Acknowledgments

The authors would like to thank Kevin Johnson, David Fazio, Jessica Zinger and Ron Cash for their assistance with field work. Funding for this research was provided by NSF-DDRI #1129889, NSF-EAR #0952242, and Geological Society of America graduate student research grant #9657-

11. This manuscript was greatly improved by reviews from Guido Zolezzi and two anonymous reviewers. The data used are listed in the references, and/or can be obtained by contacting K. Konsoer (kkonsoer@lsu.edu).

References

Abad, J.D., and Garcia, M.H., 2009a. Experiments in a high-amplitude Kinoshita meandering channel: 1. Implications of bend orientation on mean and turbulent flow structure. *Water Resources Research*, 45 (2), W02401.

Abad, J.D., and Garcia, M.H., 2009b. Experiments in a high-amplitude Kinoshita meandering channel: 2. Implications of bend orientation on bed morphodynamics. *Water Resources Research*, 45 (2), W02402.

Abbe, T.B., Montgomery, D.R., 1996. Large woody debris jams, channel hydraulics and habitat formation in large rivers. *Regulated Rivers: Research and Management*. 12, 201-221.

Bathurst, J.C., Thorne, C.R., and Hey, R.D., 1979. Secondary flow and shear-stress at river bends. *Journal of the Hydraulics Division-ASCE.* 105(10), 1277–1295.

Bennett, S.J., Wu, W., Alonso, C.V., and Wang, S.S.Y., 2008. Modeling fluvial response to in-stream woody vegetation: implications for stream corridor restoration. *Earth Surface Processes and Landforms*. 33, 890-909.

Blanckaert, K., 2010. Topographic steering, flow recirculation, velocity redistribution, and bed topography in sharp meander bends. *Water Resources Research,* 46, W11901.

Blanckaert, K., 2011. Hydrodynamic processes in sharp meander bends and their morphological implications. *Journal of Geophysical Research-Earth Surface,* 116, F01003.

Blanckaert, K., and de Vriend, H.J., 2004. Secondary flow in sharp open-channel bends. *Journal of Fluid Mechanics,* 498, 353–380.

Blanckaert, K., Duarte, A., Chen, Q., and Schleiss, A.J., 2012. Flow processes near smooth and rough (concave) outer banks in curved open channels. *Journal of Geophysical Research: Earth Surface*, 117, F04020.

Blanckaert, K., and Graf, W.H., 2001. Mean flow and turbulence in open-channel bend. *Journal of Hydraulic Engineering*, 127(10), 835-847.

Blanckaert, K., and Graf, W.H., 2004. Momentum transport in sharp open-channel bends. *Journal of Hydraulic Engineering*, 130(3), 186-198.

Daniels, M.D., and Rhoads, B.L., 2003. Influence of a large woody debris obstruction on three dimensional flow structure in a meander bend. *Geomorphology*. 51, 159-173.

Daniels, M.D., and Rhoads, B.L., 2004. Spatial pattern of turbulence kinetic energy and shear stress in a meander bend with large woody debris. In *Riparian Vegetation and Fluvial Geomorphology*. ed S.J Bennett and A. Simon, 87–97. AGU: Washington, D.C.;

Daniels, M.D., and Rhoads, B.L., 2007. Influence of experimental removal of large woody debris on spatial patterns of three-dimensional flow in a meander bend. *Earth Surface Processes and Landforms*. 32, 460-474.

Darby, S.E., Trieu, H.Q., Carling, P.A., Sarkkula, J., Koponen, J., Kummu M., Conlan, I. and Leyland, J., 2010. A physically based model to predict hydraulic erosion of fine-grained riversbanks: The role of form roughness in limiting erosion. *Journal of Geophysical Research*. 115, 1-20.

Dietrich, W.E., 1987. Mechanics of flow and sediment transport in river bends. In *River channels environment and process,* ed. K. S. Richards, 179–224. Oxford: Basil Blackwell.

Dietrich, W.E., and Smith, J.D., 1983. Influence of the point-bar on flow through curved channels. *Water Resources Research*, 19(5), 1173–1192.

Einstein, H.A., 1950. The bedload function for bedload transportation in open channel flows. *Technical Bulletin No. 1026*, USDA, Soil Conservation Service, 1-71.

Engel, F.L., and Rhoads, B.L., 2012. Interaction among mean flow, turbulence, bed morphology, bank failures and channel planform in an evolving compound meander loop. *Geomorphology*, 163(SI), 70–83.

Ferreira da Silva, A.M., Ahmari, H., 2009. Size and effect on the mean flow of large-scale horizontal coherent structures in open-channel flows: an experimental study. *Canadian Journal of Civil Engineering*. 36, 1643-1655.

Frothingham, K.M., and Rhoads, B.L., 2003. Three-dimensional flow structure and channel change in an asymmetrical compound meander loop, Embarras River, Illinois. *Earth Surface Processes and Landforms*. 28, 625-644.

Ferguson, R.I., Parsons, D.R., Lane, S.N., and Hardy, R.J., 2003. Flow in meander bends with recirculation at the inner bank. *Water Resources Research*, 39(11), 1-13.

Gorrick, S. and Rodriguez, J.F., 2012. Sediment dynamics in a sand bed stream with riparian vegetation. *Water Resources Research*. 48, 1-15.

Güneralp, İ., and Rhoads, B.L., 2008. Continuous characterization of the planform geometry and curvature of meandering rivers. *Geographical Analysis*, 40 (1), 1–25.

Güneralp, İ., and Rhoads, B.L., 2010. Spatial autoregressive structure of meander evolution revisited. *Geomorphology*, 120, 91-106.

Jackson, R.G., 1975a. A depositional model of point bars in the lower Wabash River. PhD dissertation, University of Illinois – Urbana-Champaign.

Jackson, R. G. 1975b. Velocity and bed-form texture patterns of meander bends in the lower Wabash River of Illinois and Indiana. *Geological Society of America Bulletin*, 86 (11), 1511–1522.

Jamieson, E.C., Post, G., and Rennie, C.D., 2010. Spatial variability of three-dimensional Reynolds stresses in a developing channel bed. *Earth Surface Processes and Landforms*. 35, 1029-1043.

Julien, P.Y., and Klaassen, G.J., 1995. Sand-dune geometry of large rivers during floods. *Journal of Hydraulic Engineering*, 121(9), 657-663.

Kean, J.W., and Smith, J.D., 2004. Flow and boundary shear stress in channels with woody bank vegetation. In *Riparian Vegetation and Fluvial Geomorphology*. ed Bennett and Simon, 237-252. AGU: Washington, D.C.

Kean, J.W., and Smith, J.D., 2006a. Form drag in rivers due to small-scale natural topographic features: 1. Regular sequences. *Journal of Geophysical Research*. 110, 1-13.

Kean, J.W., and Smith, J.D., 2006b. Form drag in rivers due to small-scale natural topographic features: 1. Irregular sequences. *Journal of Geophysical Research*. 111, 1-15.

Keller, E.A., and Swanson, F.J., 1979. Effects of large organic material on channel form and fluvial processes. *Earth Surface Processes*. 4, 361-380.

Konsoer, K.M., Rhoads, B.L., Langendoen, E.J., Best, J.L., Ursic, M.E., Abad, J.D., and Garcia, M.H., 2015. Spatial variability in bank resistance to erosion on a large meandering, mixed bedrock-alluvial river. *Geomorphology*, 252, 80-97.

Lauer, J. 2012 National Center for Earth-Surface Dynamics, http://www.nced.umn.edu/content/stream-restoration-toolbox

Magna, M., and Kirchner, J.W., 2000. Stress partitioning in streams by large woody debris. *Water Resources Research*. 36(8), 2373-2379.

Parker, G. and Andrews, E.D., 1986. On the time development of meander bends. *Journal of Fluid Mechanics*, 162, 139-156.

Parsons, D. R., Jackson, P.R., Czuba, J.A., Engel, F.L., Rhoads, B.L., Oberg, K.A., Best, J.L., Mueller, D.S., Johnson, K.K., and Riley, J.D., 2012. Velocity Mapping Toolbox (VMT): A processing and visualization suite for moving-vessel aDcp measurements. *Earth Surface Processes and Landforms*. 38(11), 1244–1260.

Pizzuto, J.E., and Meckelnburg, T.S., 1989. Evaluation of a linear bank erosion equation. *Water Resources Research*, 25(5), 1005-1013.

Rhoads, B. L., and Kenworthy, S.T., 1998. Time-averaged flow structure in the central region of a stream confluence. *Earth Surface Processes and Landforms*, 23(2), 171–191.

Rhoads, B.L., and Welford, M.R., 1991. Initiation of river meandering. *Progress in Physical Geography*. 15(2), 127-156.

Robinson, E.G., and Beschta, R.L., 1990. Coarse woody debris and channel morphology interactions for undisturbed streams in southeast Alaska, U.S.A. *Earth Surface Processes and Landforms*. 15, 149-156.

Rozovskii, I. L. 1957. *Flow of water in bends of open channels*. Kiev, U.S.S.R.: Academy of Sciences of the Ukraninian S.S.R.

Shields, F.D., Morin, N., and Kuhnle, R.A., 2001. Effects of large woody debris structures on stream hydraulics. In *Proceedings of the 2001 Wetlands Engineering and River Restoration Conference*, ed. D.F. Hayes, American Society of Civil Engineers, Reston, VA.

Sukhodolov, A.N., and Sukhodolova, T.A., 2010. Case Study: Effect of submerged aquatic plants on turbulence structure in a lowland river. *Journal of Hydraulic Engineering*. 136(7), 434-446.

Szupiany, R.N., Amsler, M.L., Best, J.L., and Parson, D.R., 2007. Comparison of fixed- and moving-vessel flow measurements with an aDcp in a large river. *Journal of Hydraulic Engineering*. 133(12), 1299-1309.

Termini, D., 2009. Experimental observations of flow and bed processes in large-amplitude meandering flume. *Journal of Hydraulic Engineering-ASCE*, 135(7), 575–587.

Termini, D., and Piraino, M., 2011. Experimental analysis of cross-sectional flow motion in a large amplitude meandering bend. *Earth Surface Processes and Landforms*. 36, 244-256.

Thorne, C.R., 1992. Bend scour and bank erosion on the meandering Red River, Louisiana. In *Lowland Floodplain Rivers: Geomorphological Perspectives*. ed. P.A. Carling and G.E. Petts, 95-115. John Wiley & Sons, Ltd.

Thorne, S.D., and Furbish, D.J., 1995. Influences of coarse bank roughness on flow within a sharply curved river bend. *Geomorphology*. 12, 241-257.

Thorne, C.R., and Hey, R.D., 1979. Direct measurements of secondary currents at a river inflection point. *Nature*, 280(5719), 226–228.

Thorne, C.R., Zevenbergen, L., Pitlick, J., Rais, S., Bradley, J.B., and Julien, P., 1985. Direct measurements of secondary currents in a meandering sand-bed river. *Nature*, 315(27), 746–747.

Whiting, P.J., and Dietrich, W.E., 1993a. Experimental studies of bed topography and flow patterns in large-amplitude meanders: 1. Observations. 29(11), 3605-3614.

Whiting, P.J., and Dietrich, W.E., 1993b. Experimental studies of bed topography and flow patterns in large-amplitude meanders: 2. Mechanisms. *Water Resources Research*. 29(11), 3615-3622.

Young, W.J., 1991. Flume study of the hydraulic effects of large woody debris in lowland rivers. *Regulated Rivers: Research and Management*. 6, 203-211.

Zong, L., and Nepf, H., 2011. Spatial distribution of deposition within a patch of vegetation. *Water Resources Research*. 47, 1-12.